Brazil-USA Collaborative Research: Modifications by Anthropogenic Pollution of the Natural Atmospheric Chemistry and Particle Microphysics of the Tropical Rain Forest During the GoAmazon Intensive Operating Periods (IOPs)

S. Martin: Register#: ER65578, SC#: DE-SC0011115
J. Jimenez: Register#: ER65580, DE-SC0011105
S. Kim: Register#: ER65579, DE-SC0011122

Final Report

August 2017

Contributors: Scot Martin (DOE, PI), Jose Jimenez (DOE), Saewung Kim (DOE), James Smith (DOE), Rodrigo Souza (FAPEAM, co-PI), Henrique Barbosa (FAPESP, co-PI)

Manaus, a city of nearly two million people, represents an isolated urban area having a distinct urban pollution plume within the otherwise pristine Amazon Basin. The plume has high concentrations of oxides of nitrogen and sulfur, carbon monoxide, particle concentrations, and soot, among other pollutants. Critically, the distinct plume in the setting of the surrounding tropical rain forest serves as a natural laboratory to allow direct comparisons between periods of pollution influence to those of pristine conditions. The funded activity of this report is related to the Brazil-USA collaborative project during the two Intensive Operating Periods (wet season, 1 Feb - 31 Mar 2014; dry season, 15 Aug - 15 Oct 2014) of GoAmazon2014/5. The project addresses key science questions regarding the modification of the natural atmospheric chemistry and particle microphysics of the forest by present and future anthropogenic pollution.

The **first objective** of the project was to understand and quantify the interactions of biogenic and anthropogenic emissions with respect to the production of secondary organic material. In clean conditions in the Amazon basin, secondary organic material dominates the diameter distribution of the submicron particles. How and why is the diameter distribution shifted by pollution? The second objective followed from the first in that, although the diameter distribution is dominated by secondary organic material, the actual source of new particle production remains uncertain (i.e., the number concentration). The **second objective** was to test the hypothesis that new particles under natural conditions are produced as a result of evaporation of primary particles emitted by fungal spores as well as to investigate any shifts in this mechanism under pollution conditions, e.g., in consequence to the high concentrations of SO_2 in the pollution plume. Combined, the number-diameter distribution is the key connection to upscaling to the effects of

aerosol particles on clouds and climate. Understanding this upscaling under clean and pollution conditions, including differences, was the **third objective**.

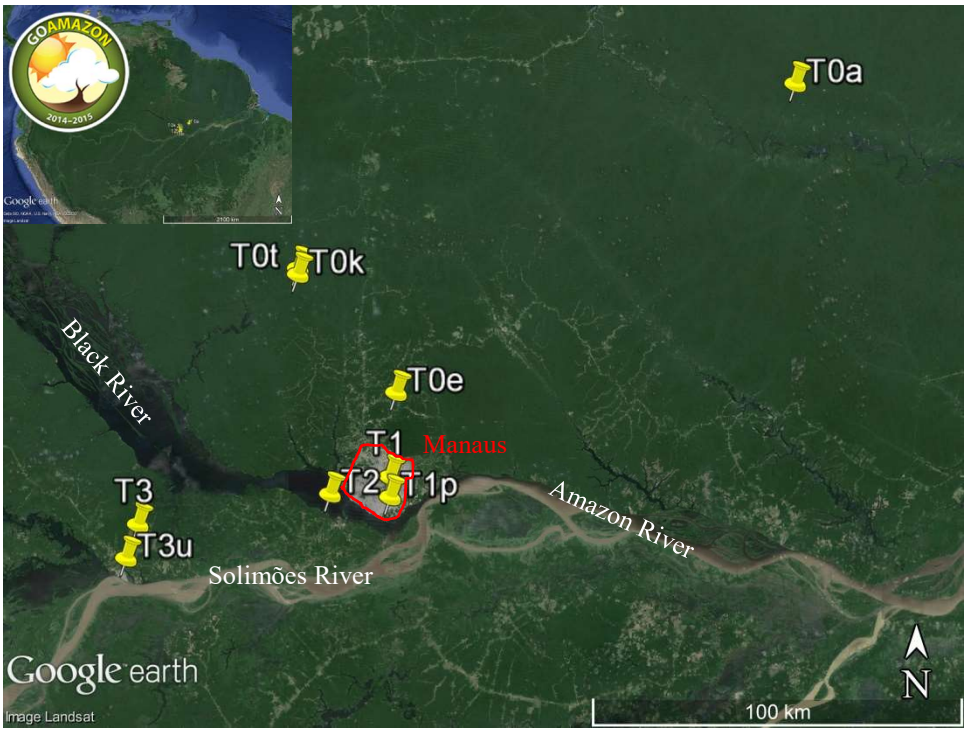

Locations of GoAmazon2014/5 research sites in the environs of the city of Manaus (-3.1°, -60.0°) in the state of Amazonas in the country of Brazil. Manaus is located at the confluence of the Black River ("Rio Negro") with the Solimões River, which together form the Amazon River. The inset shows the location of the experimental domain within South America. For prevailing winds, Manaus is on the order of 1200 km (IOP1) to 1600 km (IOP2) from the Atlantic Ocean.

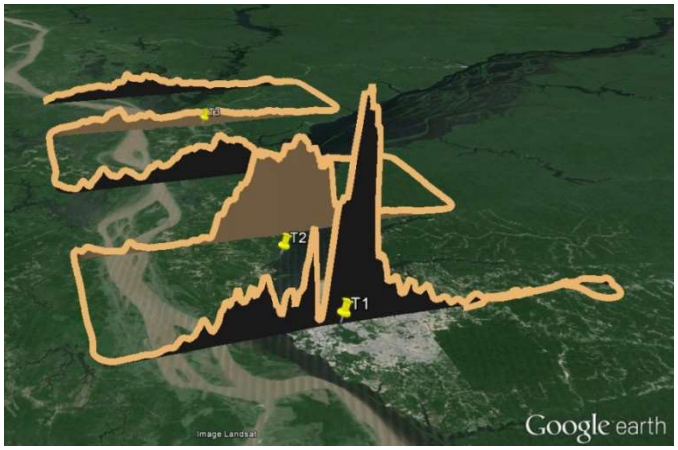

Particle concentrations measured by an airbone cloud condensation particle counter aboard the G1 research aircraft, GoAmazon2014/5, IOP1, 16 March 2014, 14:41 to 15:49 UTC. The image maps the pollution plume from Manaus to the west over the forest.

Aerial view of research site T3.

Objective 1

Understanding and quantify the interactions of biogenic and anthropogenic emissions with respect to the production of organic particular matter (PM_1)

Part 1. Activities led by **Scot Martin** (Harvard University, funded by DOE).

A Proton-Transfer-Reaction Time-of-Flight Mass Spectrometer (PTR-TOF-MS), housed within MAOS container, was operated at T3 during the IOPs. The scientific goal was to elucidate the major BVOC products that occur under clean compared to anthropogenic conditions. Measured compounds included many biogenic hydrocarbons (e.g., isoprene, monoterpenes, sesquiterpenes), anthropogenic hydrocarbons (e.g., benzene, toluene, C8-aromatics, C9-aromatics), and their oxidation products. A cold trap at a temperature of -40 °C was deployed upstream of the PTR-TOF-MS for separation and differential classification of BVOC oxidation products. In particular, isoprene hydroperoxides could be removed by the cold trap, whereas methyl viniyl ketone (MVK) and methacrolein (MACR) were not trapped. These compounds are the dominant first-generation oxidation products via the HO_2 and NO pathway of isoprene photoxidation, respectively, all producing the $C_4H_7O^+$ ion upon the reaction with H_3O^+.

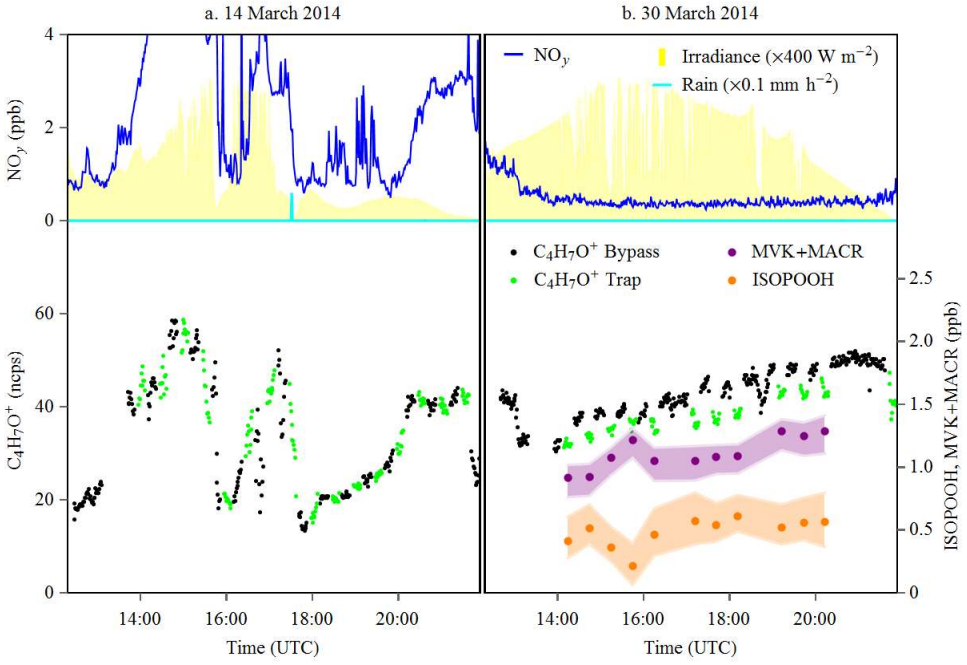

Figure 1.1 Example time series of NO_y concentrations (top) and signal intensities of $C_4H_7O^+$ ions (bottom) on (a) 14 March 2014 and (b) 30 March 2014, representing polluted and clean conditions, respectively. Top panels also show shortwave broadband total downwelling irradiance (W m^{-2}, yellow shadow) and rain amount (mm hr^{-1}, cyan line). The black and green points in the bottom panels show $C_4H_7O^+$ signal intensities measured through and bypass the trap, respectively. The purple and orange points represent the median concentration of MVK+MACR and ISOPOOH, respectively. The light purple and light orange represent the respective interquartile range. Local noon is at 16:00 UTC.

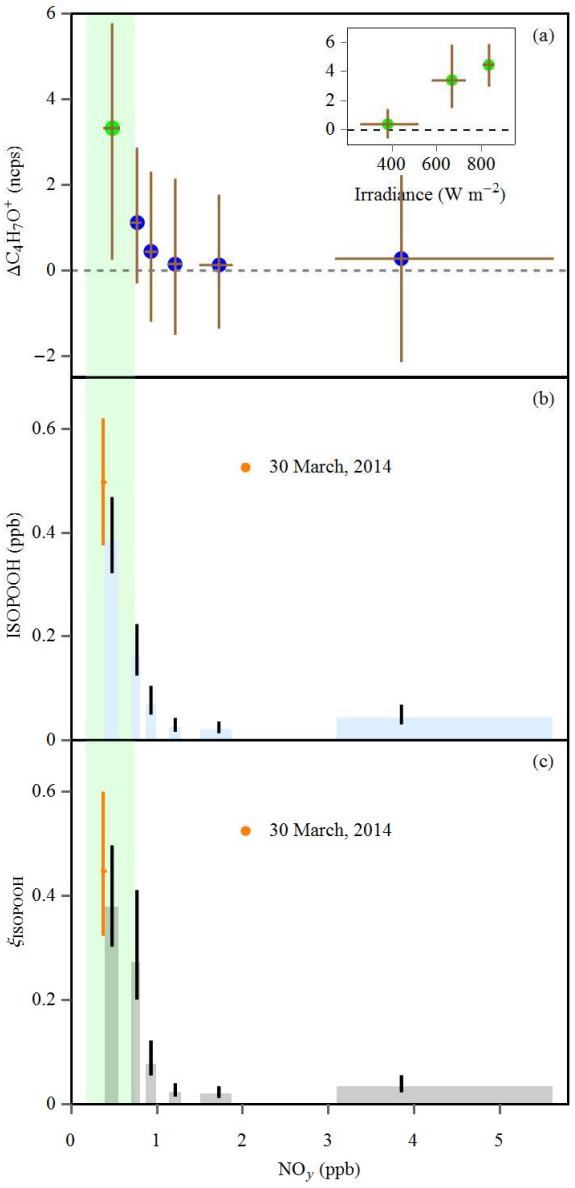

Figure 1.2. Dependence on NO_y concentration of (a) the intensity difference, $\Delta C_4H_7O^+$, of $C_4H_7O^+$ ion through and bypass the trap, (b) ISOPOOH concentration calculated using median value of $\Delta C_4H_7O^+$, and (c) concentration ratio $\xi_{ISOPOOH}$ of ISOPOOH and MVK + MACR. The whole data set of $\Delta C_4H_7O^+$ is divided into 6 equal-sized subsets based on NO_y concentrations. The dots (a) and bar heights (b and c) represent the median of each subset and the sticks represent the interquartile ranges. Inset figure shows the dependence of $\Delta C_4H_7O^+$ in the first sextile of the data set on mean irradiance of previous 3 hours. The light green region represents the NO_y concentration range for unpolluted condition over central Amazonia.

The obtained data set provides a unique perspective regarding how anthropogenic pollution can change oxidation products and reaction pathways of isoprene chemistry over Amazonia. Figure 1.1 compares the time series of measured trap and bypass signal intensities of the $C_4H_7O^+$ ion for two different days. These two days were selected as examples of contrasting behavior during times of low and high NO_y. On 14 March 2014, the NO_y concentrations were regularly above 1 ppb. The trap and bypass intensities followed each other closely, without any statistically significant differences. The agreement of the trap and bypass measurements of $C_4H_7O^+$ during this day suggests that the bypass $C_4H_7O^+$ signals predominantly arose from MVK and MACR without any contribution by ISOPOOH. In comparison, on 30 March 2014 the NO_y concentration at T3 varied little from 0.4 ppb from mid-morning through sunset. The $C_4H_7O^+$ intensity measured with the trap was lower than that measured with the bypass. This difference indicates that lower-volatility compounds present at low-NO condition and detected as $C_4H_7O^+$, consistent with ISOPOOH, were removed by the trap.

The attribution of intensity differences $\Delta C_4H_7O^+$ between the bypass and the trap to ISOPOOH is further supported by the dependence of $\Delta C_4H_7O^+$ on NO_y concentration and irradiance revealed from the whole data set. Since ISOPOOH isomers are photooxidation products of isoprene via the HO_2 pathway, higher ISOPOOH concentrations are expected at lower NO_y concentration, because of increased contribution of HO_2 pathway to ISOPOO fate, and at higher irradiance, because of higher OH concentration and isoprene emission. As shown in Figure 1.2a, for subsets of $NO_y > 1$ ppb, $\Delta C_4H_7O^+$ medians are close to zero. By comparison, for subsets having $NO_y < 1$ ppb, $\Delta C_4H_7O^+$ medians increase for decreasing NO_y. As shown in the inset of Figure 2a, the median of $\Delta C_4H_7O^+$ increased as the irradiance increased, from 0.4 ncps at 380 W m^{-2} to 4.5 ncps at 830 W m^{-2}.

The concentrations of ISOPOOH and MVK+MACR are determined from measured trap and bypass $C_4H_7O^+$ signals based on calibration using authentic (1,2)-ISOPOOH and MVK standards. Figures 1.2b and 1.2c present the ISOPOOH concentrations determined from the $\Delta C_4H_7O^+$ medians in Figure 1.2a and the corresponding ratio $\xi_{ISOPOOH}$ of ISOPOOH concentration to the total concentration of MVK and MACR. Consistent with the dependence of the median $\Delta C_4H_7O^+$ on NO_y (Figure 1.2a), the ISOPOOH concentration and $\xi_{ISOPOOH}$ increased for decreasing NO_y for subsets having $NO_y < 1$ ppb (Figure 1.2b). Figures 1.2b and 1.2c also show the measured results on 30 March 2014 (NO of 0.37 ppb), which follows the dependence on NO_y revealed from the full data set and extends it to the lower bound of observed NO_y concentration.

The measurements provide observational constraint to isoprene chemistry under clean condition. The mean NO_y concentration for unpolluted air over central Amazonia was previously reported as 0.45 ± 0.28 (2σ) ppb in the wet season. The observation on 30 March (NO_y of 0.38 ± 0.06 pbb) as well as for the minimum NO_y bin (0.33-0.63 ppb), therefore, represent background conditions over central Amazonia. For the minimum NO_y bin (0.48 ppb), the median in $\xi_{ISOPOOH}$ was 0.38 and the interquantile range was 0.30-0.49. For 30 March 2014, and the median and interquartile range was 0.45 and 0.33-0.60, respectively. These $\xi_{ISOPOOH}$ values are significantly smaller than the simulated $\xi_{ISOPOOH}$ over central Amazonia (on average 1.2) by global model. The difference between model prediction and the current observation suggests that global transport model overpredicts the importance of the HO_2 pathway under clean conditions by a factor of two and hence can be biased when predicting the associated climate effects (esp. production organic particulate matter) in a global scale.

In the future, the Amazon basin will continue to experience land use change and urbanization. One direct effect of the intensified human activities is increased emission of NO_x. As shown in Figure 1.2, the product distribution represented as $\xi_{ISOPOOH}$ is sensitive to increases in NO_y concentration in its lower range. A small increase in NO concentration from the background level can lead to a large increase in the fraction reacting by the NO pathway and a large decrease in the contributions of other pathways including the HO_2 pathway. The difficulty to evaluate possible anthropogenic influence on isoprene chemistry is to understand the fate of ISOPOO radicals under the clean or background condition, whereas NO pathway dominates under polluted condition. By constraining the fraction reacting by the HO_2 pathway under clean tropical conditions, the current observational results delimit the extent to which human activity can affect the distribution of primary isoprene oxidation products. Due to their differing chemical reactivity, atmospheric lifetimes, and potential to form secondary organic material, the nature of the products formed is crucial in determining the net effects of isoprene chemistry on the oxidative capacity and radiative properties of the atmosphere.

A High-Resolution Time-of-Flight Aerosol Mass Spectrometer (HR-ToF-AMS, hereafter AMS; owned by EMSL) was deployed to T3 during both IOPs. The scientific goal was the measurement of the composition of submicron aerosol particles to understand the sources and fates of the atmospheric particle population, and the effects of anthropogenic pollution on the same. More specifically, the AMS provides information on the mass spectral characteristics of the particles, which, especially when coupled to other gas and particle-phase measurements, is a

powerful tool for the investigation of atmospheric secondary organic material. The atmospheric chemistry of isoprene contributes to the production of a substantial mass fraction of the particulate matter (PM) over tropical forests. Isoprene epoxydiols (IEPOX) produced in the gas phase by the oxidation of isoprene under HO_2-dominant conditions are subsequently taken up by particles, thereby leading to production of secondary organic PM. Anthropogenic influences, namely enhanced sulfate and associated volume and acidity, as well as NO_x emissions, can alter this mechanism and therefore affect the production of IEPOX-derived PM. The present study investigated possible perturbations to this pathway by urban pollution.

Measurements at the T3 site, during the wet season of 2014 (IOP1), were employed to investigate this scientific question. Mass spectra of organic PM collected with an Aerodyne Aerosol Mass Spectrometer were analyzed by positive-matrix factorization (PMF). One resolved statistical factor ("IEPOX-SOA factor") was associated with PM production by the IEPOX pathway. The IEPOX-SOA factor loadings correlated with independently measured mass concentrations of tracers of IEPOX-derived PM, namely C_5-alkene triols and 2-methyltetrols (R^2 = 0.96 and 0.78, respectively).

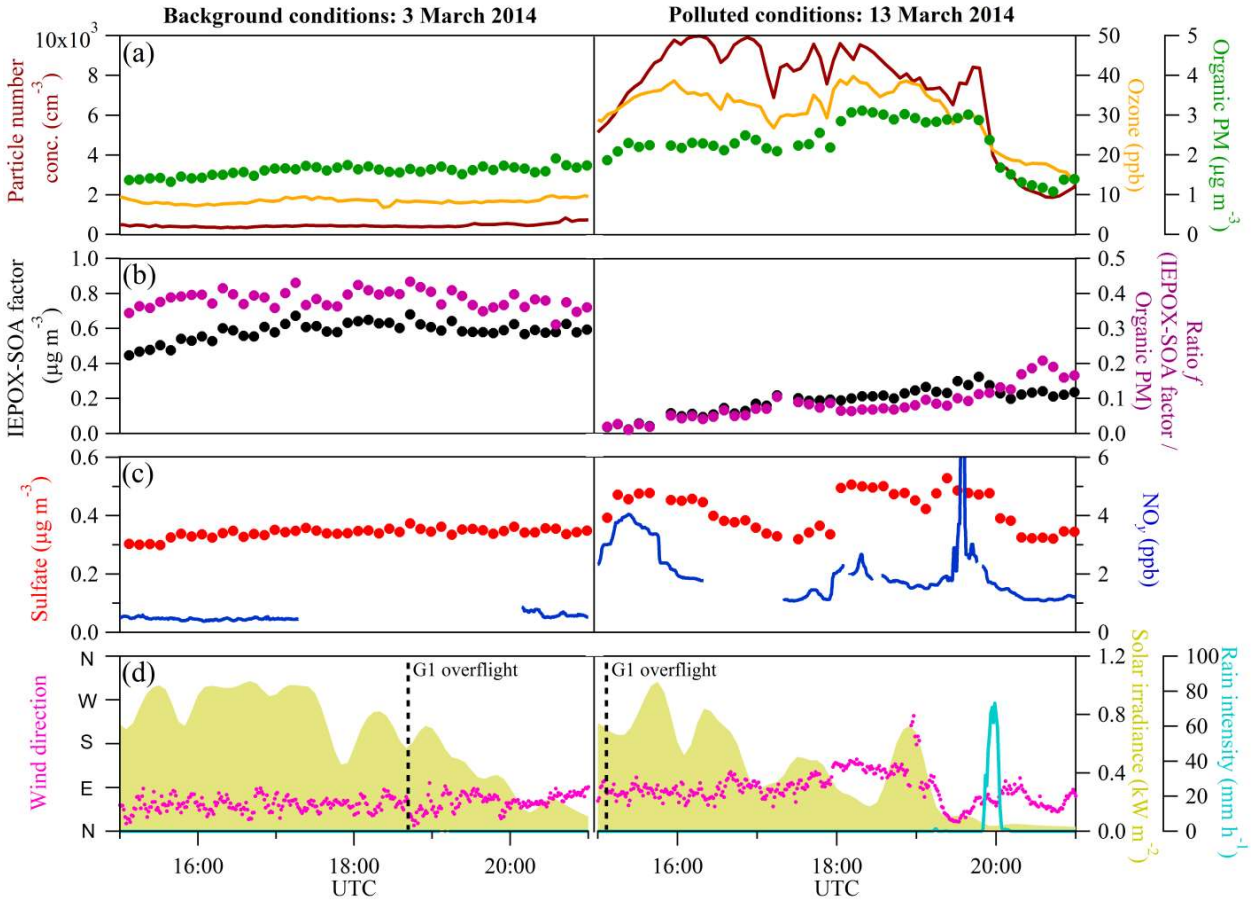

Figure 1.3. Case studies of (left) background and (right) polluted air masses passing over T3 on afternoons of 3 and 13 March 2014. (a) Ozone, particle number, and organic mass concentration. (b) IEPOX-SOA factor loading and the ratio *f* of the factor loading to the organic PM concentration. (c) Sulfate and NO_y concentrations. (d) Wind direction, rain intensity, and solar irradiance. Local time is UTC minus 4 h. Time points of overflights at 500 m by the G-1 research aircraft are marked by the dashed line.

Two case studies for background and polluted conditions observed at ground level at the T3 site are plotted in Figure 1.3. On the afternoon of 3 March, ozone concentrations were below 10 ppb, particle number concentrations were below 1000 cm^{-3}, NO_y concentrations were less than 1 ppb, and sulfate concentrations were 0.3 to 0.4 μg m^{-3}. Species concentrations were stable throughout the afternoon. In contrast, on 13 March, ozone concentrations exceeded 30 ppb for most of the afternoon, particle concentrations reached 10 000 cm^{-3}, NO_y concentrations consistently exceeded 1 ppb, and sulfate concentrations were 0.3 to 0.6 μg m^{-3}. Concentrations fluctuated markedly throughout the afternoon on 13 March, reflecting different levels of pollution influence in the air passing over the T3 site during that period. Elevated concentrations of ozone, particle number, and NO_y were reliable markers of pollution influence over the course of the study period. Pollution was associated with stronger relative enhancements in NO_y concentrations than in sulfate concentrations. With respect to the IEPOX-SOA factor, Figure 1.3 shows that the absolute and relative loadings decreased for the polluted compared to background conditions. Relative loadings are expressed by the ratio *f* of IEPOX-SOA factor loading to the organic PM mass concentration.

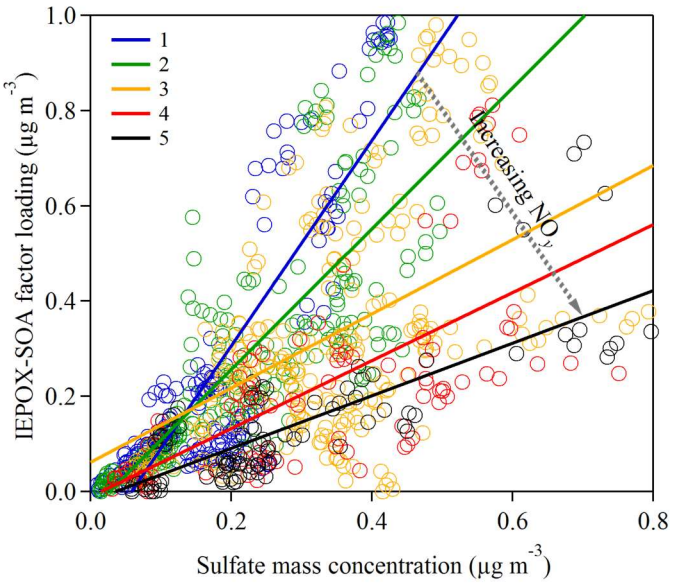

Figure 1.4. Scatter plot of sulfate mass concentration and IEPOX-SOA factor loading for local afternoon (12:00–16:00 local time; 16:00–20:00 UTC). The data sets were collected into five subsets, colored and labeled 1 to 5, based on increasing NO_y concentration.

A scatter plot between sulfate mass concentrations and IEPOX-SOA factor loadings for all afternoon periods is shown in Figure 1.4. Conditions ranging from background to polluted are represented in the data set. The visualization shows that sulfate concentration served as a first-order predictor of the IEPOX-SOA factor loading, explaining 37% of the variability. The explanation can be a combination of increased acidity, greater reaction volume including by enhanced hygroscopic growth, and possibly a nucleophilic role for sulfate in the uptake reaction. After segregation of the dataset into subsets based on NO_y concentration, as shown by different colors in Figure 1.4, the sulfate concentration explained up to 75% of the variability. The NO_y concentration measured at T3 served as a surrogate for the integrated exposure of the air mass to NO chemistry between Manaus and T3. The groups 1 to 5, representing low to high NO_y concentrations, show that enhanced NO_y concentrations act to decrease the loadings of the IEPOX-SOA factor.

Under polluted conditions, NO concentrations can be sufficiently high that ISOPOO radicals react almost entirely with NO in place of HO_2, thereby largely producing methacrolein (MACR) and methyl vinyl ketone (MVK) in place of ISOPOOH. As a result, IEPOX production can be greatly decreased, ultimately reducing PM production by IEPOX pathways. Considering both the influence of sulfate and NO chemistry, the data sets show that the suppressing effects of

increased NO concentrations often dominated over the enhancing effects of higher sulfate concentrations. In this light, increased emissions of nitrogen oxides, as anticipated for some scenarios of Amazonian economic development, could significantly alter pathways of PM production that presently prevail over the tropical forest, implying changes to air quality and regional climate.

Part 2. Activities led by **Jose Jimenez** (Univ. Colorado, Boulder, funded by DOE)

In conjunction with the HR-ToF-AMS deployment described above, a Thermal Denuder (TD), and two Oxidation Flow Reactors (OFR; including supporting O_3, CO, RH analyzers) were deployed upstream of the AMS and SMPS during both IOPs. In the OFRs, ambient air was exposed to high concentrations of hydroxyl radicals (OH) or O_3 (hereafter OH-OFR or O_3-OFR) to simulate several hours to weeks of equivalent atmospheric exposure. Additionally, a PTR-TOF-MS was used to sample the outflow of the OFR on a regular cycle during both IOPs, allowing for better quantification of the oxidative exposure within the OFR as well as information on the gas-phase oxidation products formed. Also, for a week period during the dry season, the particle output of the OH-OFR was size-selected by a DMA, followed by a CCN counter, to characterize particle hygroscopicity as a function of aging. Finally, during the end of IOP1 and between IOPs, one of the OFRs was installed at T2 and coupled to an ACSM, SMPS and PTR-MS to collect similar measurements to the T3 OFR measurements. These measurements allowed for investigation of the production and aging of organic PM_1 at a site closer to anthropogenic emission sources as well as at a location sometimes upwind of T3, potentially providing information on photochemical processing between T2 and T3.

The scientific goal of these activities was to identify and quantify contributions of important precursors of organic PM_1 (dominated by organic aerosol, OA) and understand the possibility for further regional aging and anthropogenic effects beyond T3 in the Amazon basin. A further goal using a thermodenuder setup was to explore the volatility of organic PM_1, which has important implications for evolution and lifetimes of PM_1.

Figure 1.5 presents overviews of the evolution of organic PM_1 in the OFR at T2 and T3 as a function of photochemical age (equivalent days). At lower ages, additional PM_1 is produced from biogenic VOCs (BVOC), anthropogenic VOCs (AVOC), and/or other gas-phase SOA precursors (e.g., oxidation products) in the ambient air. At increasing ages, less PM_1 is produced. For the highest ages, net particle mass loss and reduced diameters are observed. These results demonstrate the interplay among functionalization/condensation and fragmentation/volatilization during the production of PM_1 vs. heterogeneous oxidation of PM_1. Although such behavior is qualitatively similar to observations made in other campaigns in very different environments, there are important differences in the degree of oxidation required to balance production and destruction for the GoAmazon2014/5 data set. Greater production of PM_1 by OH-OFR oxidation was observed during both seasons and sites during the night than during the day, possibly because the reservoir of unreacted atmospheric gases is greater in the absence of sunlight and in the shallower nighttime boundary layer. At both sites, a maximum of approximately 4–5 times

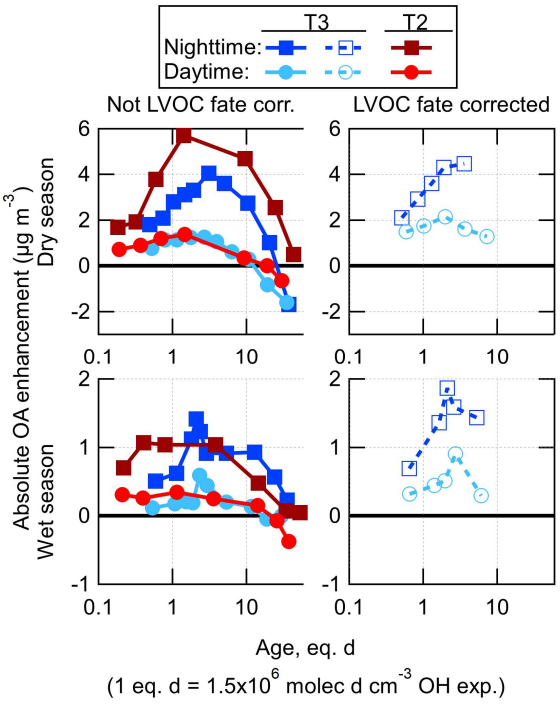

Figure. 1.5. Absolute OA enhancement after OH oxidation in the OFR as a function of photochemical age, shown as binned averages for the wet (bottom) and dry (top) seasons at both the T2 and T3 measurement sites, and split into daytime (06:00–18:00 LT) and nighttime (18:00–06:00 LT) data. This data is shown both not corrected (left) and corrected (right) for low-volatility VOC (LVOC) fate. The LVOC fate correction is applied to correct for other fates of condensable gases produced than condensation to particles that occur in the OFR which would not be expected in the atmosphere (measurements were not available for such corrections at T2, although it was likely similar). The average ambient OA concentrations during the measurement times used here were 1.2 μg m^{-3} and 6.9 μg m^{-3} at T2 in the wet and dry seasons, and 1.3 μg m^{-3} and 9.5 μg m^{-3} at T3 in the wet and dry seasons, respectively.

more SOA was formed from ambient air during the dry season than the wet season. The maximum amount of SOA formed at the T2 site during nighttime in the dry season was about 50% larger than during nighttime in the wet season. It may be the case that this increased SOA formation was due to a larger anthropogenic source strength in the closer proximity to the city of Manaus. The maximum amounts of SOA formed at all other times were approximately equivalent at each site. These measurements suggest that the seasonal changes in SOA precursor gases are more important than the proximity to Manaus. One possibility is that a substantial fraction of the anthropogenic SOA had already formed by the time the air passed over the T2 site, so formation in the OFR of the remaining potential SOA did not lead to a very large difference between the sites sources. Also for the OH-OFR for all sites/seasons/time-of-day as age was increased, the degree of oxidation of the PM_1 likewise increased, as evidenced in trends in the O:C and H:C elemental ratios (not shown).

As shown in Figure 1.6, approximately 2–3 times more SOA was formed from O_3 oxidation during the dry season than the wet season, again with typically higher formation during nighttime than daytime hours. The amount of SOA formation increased with O_3 atmospheric equivalent age (eq. age), with maximum values above approximately 1 eq. day of O_3 oxidation. This is consistent with the age at which the ambient MT (and likely other compounds) were all reacted. As observed previously at another biogenic site, O_3 oxidation of ambient air produced at most ~ 1/6th of the SOA that was formed from OH.

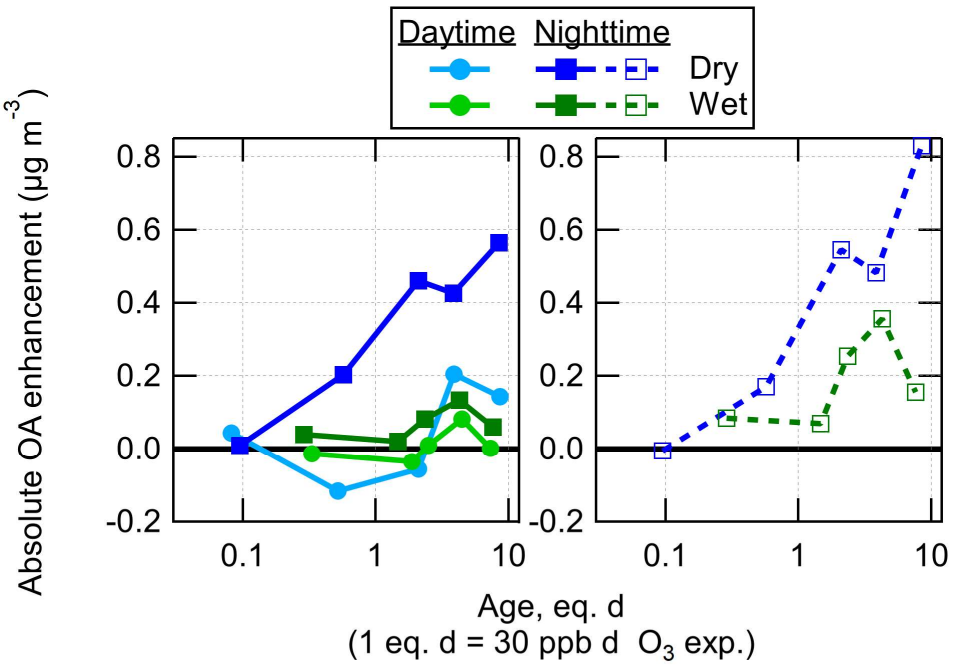

Figure 1.6. Absolute OA enhancement after O_3 oxidation in the OFR as a function of photochemical age, shown as binned averages for the wet and dry seasons at the T3 measurement site, and split into daytime (06:00–18:00 LT) and nighttime (18:00–06:00 LT) data. This data is shown both not corrected (left) and corrected (right) for LVOC fate.

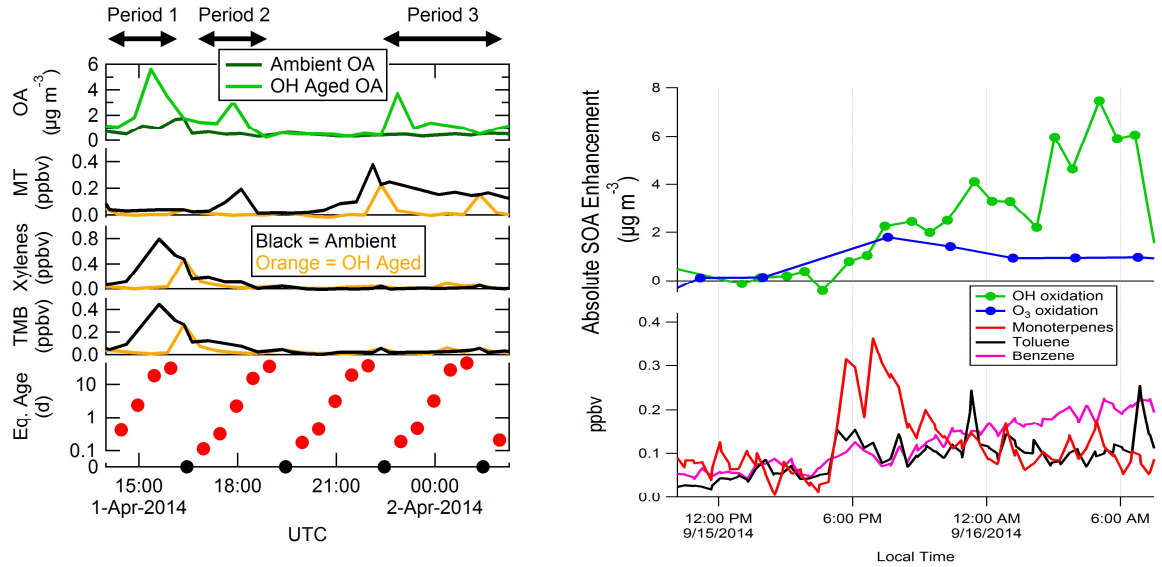

Figure. 1.7. (Left) An example of OA concentrations in ambient air and after OH oxidation of ambient air in the OFR at the T2 site, shown together with MT, xylenes, and trimethylbenzene (TMB) measured in ambient air and after OH oxidation. The OH exposure is also shown (in eq. days). OH age was cycled through a range of exposures, including no added exposure (black circles) where none of the VOCs were reacted in the OFR. This example illustrates how SOA formation in the OFR can come from anthropogenic (Period 1), biogenic (Period 3), or mixed (Period 2) precursors, depending on ambient conditions. **(Right)** Comparison of the time series of OA enhancement in the OH-OFR and O_3-OFR (and ambient BVOC and AVOC gases), where generally the OH-OFR SOA production tracks AVOC (and BVOC) tracers while the O_3-OFR primarily tracks BVOC tracers.

Figure 1.7 shows ~one-day time series of PM_1 production within the OFR for IOP1 (left) and IOP2 (right). For the IOP1 period shown, PM_1 production in the OFR was at times concurrent with elevated ambient AVOC measurements, at other times with BVOCs, and sometimes when both BVOCs and AVOCs were present. This result demonstrates that PM_1 production was controlled by variable anthropogenic, biogenic, and mixed sources during different periods. The amount of different VOCs that are reacted at different OH exposures in the OFR can be seen by comparing the ambient and OFR-processed concentrations. For the IOP2 period shown, PM_1 production for the OH-OFR tracks mostly anthropogenic tracers while in the O_3-OFR they track primarily track biogenic tracers, demonstrating the large differences that the types of oxidants exert on PM_1 formation for different air mass compositions.

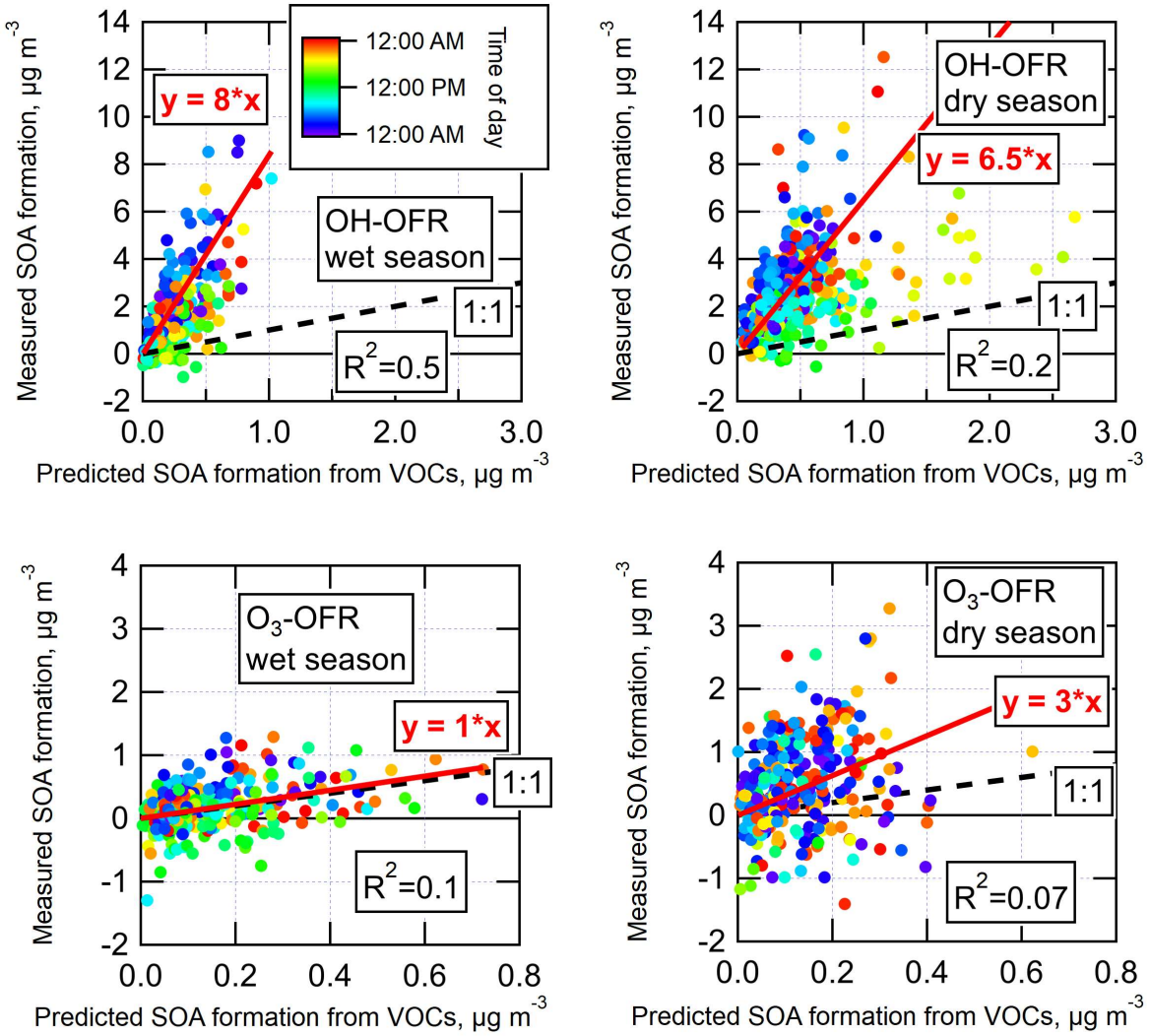

Figure. 1.8. Measured SOA formation vs. the concentration of SOA predicted to form from the oxidation of ambient VOCs, shown for OH and O_3 oxidation during both wet and dry seasons. Regression lines and correlation coefficients are shown for each OFR type and season. Data are colored by local time of day. Measured SOA formation is corrected for LVOC fate.

The measured SOA formation (at the eq. ages of maximum SOA production) from ambient air in the OFR is shown in Figure 1.8, for both wet (IOP1) and dry (IOP2) seasons and both OH and O_3 oxidation and with linear regressions shown. The predicted SOA formation was estimated by applying typical chamber SOA yield values to measured ambient VOC concentrations. OH oxidation of ambient air produced on average 6.5–8 times more SOA than could be accounted for from ambient VOCs. This is consistent with previous OFR measurements, suggesting that typically unmeasured ambient gases play a substantial role in ambient SOA formation from OH oxidation. The amount of SOA formed from O_3 oxidation was on average similar or slightly larger than the amount that could be explained from measured ambient VOCs. This measurement is noisy (particularly in the dry season, when using a difference measurement to quantify several tenths of μg m^{-3} of SOA formation on top of ~10–20 μg m^{-3} is difficult). Given the uncertainties in e.g. VOC speciation and yield, it is consistent with the previous OFR measurements in a pine forest where ambient VOCs could explain all SOA formation from O_3 oxidation. These non-VOC ambient gases are likely to be the typically unmeasured/unspeciated class of lower volatility S/IVOCs. Unfortunately, there were no instruments dedicated to quantifying the total concentration of these gases during GoAmazon2014/5. The measurement of such gases remains a critical gap in our understanding of the lifecycle of carbon in the atmosphere. However, the SOA formed in the OFR that cannot be accounted for by VOCs is effectively an integrated measure of these S/IVOC gases (multiplied by their SOA yield). They are measured by first converting them into SOA, which is much more readily measureable and quantifiable than S/IVOCs with current instrumentation.

Whereas the slope of the measured vs. predicted SOA formation from pine forest air was roughly constant at approximately 4, the slope of the measured vs. predicted SOA formation from OH oxidation in the Amazon varied as a function of time of day. Analysis of the diurnal cycles of

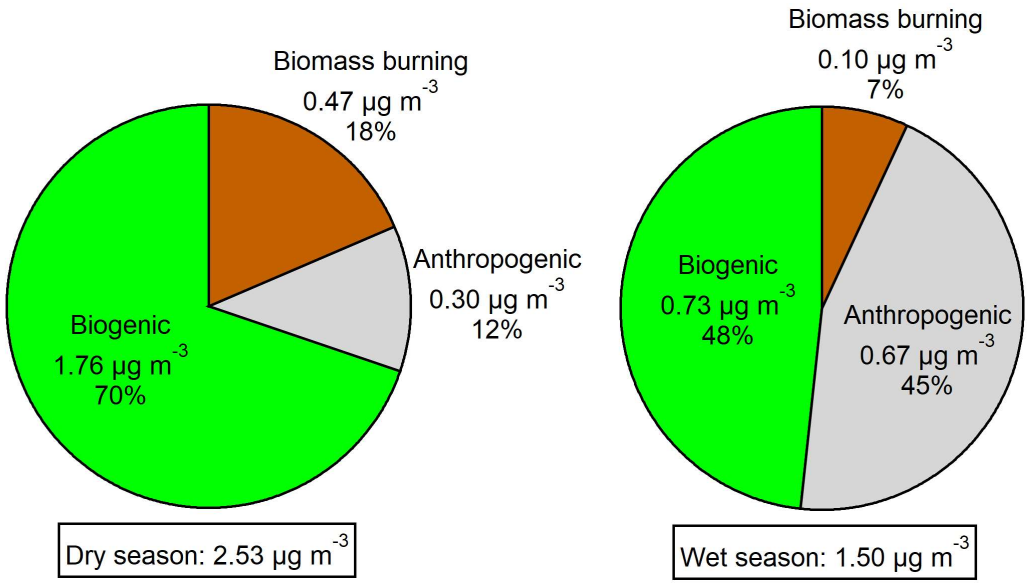

Figure 1.9. Amounts and fractions of the total SOA formation from OH oxidation in the OFR at the T3 site that were attributed to biogenic, anthropogenic, and biomass burning emission types using multilinear regression analysis.

measured and predicted SOA formation showed that the predicted SOA was on average slightly lower during nighttime than during daytime. The cycle of measured SOA formation was the opposite, leading to slopes (in Figure 1.8) that were lowest during daytime and highest in the hours before sunrise. The reasons for the observed trends are unclear, but likely result from the confluence of several processes, e.g., diurnal changes in emission and concentration profiles (of VOCs and/or S/IVOCs), boundary layer dynamics, and varying ambient oxidant concentrations.

The results of the OFR modeling (discussed above) led to the conclusion that a dominant fraction of the SOA formation potential from oxidation of ambient air by OH, particularly during nighttime hours, was derived from gases that were not speciated or quantified during this campaign. Also, these gases could form SOA upon OH oxidation, but little or no SOA after O_3 oxidation, suggesting they tended not to contain C=C bonds. These conclusions are consistent with previous measurements of the oxidation of ambient air in an OFR in pine forest air in the US Rocky Mountains and in urban outflow downwind of Los Angeles. In the analyses of the pine forest measurements, it was found that the unmeasured SOA-forming gases were likely to be S/IVOCs. Because the measured SOA formation correlated well with ambient MT, it was likely that the S/IVOCs were biogenic oxidation products (or were at least co-emitted with MT). With respect to ambient SOA-forming gases, the rural pine forest air system was relatively simple and was generally dominated by biogenic, terpene-related gases.

Despite that a measurement of the total concentration of S/IVOCs during GoAmazon2014/5 was not available (as is typical for most field campaigns at present), we can still extract information about the main sources contributing to the SOA formation potential from S/IVOCs present in ambient air by comparing with available VOC and/or tracer measurements. In that analysis, we made the assumption that the conclusion from the pine forest measurements, specifically that VOCs and S/IVOCs from a given emission type correlate well with tracers from that same source, will also apply to all of the emission types at the T3 site. The T3 site was chosen because it was expected to be impacted by multiple types of emissions. These include regional biogenic emissions (isoprene, MT, SQT, etc.), anthropogenic emissions from the city of Manaus and other towns and roads closer to the site, and local and regional biomass burning emissions. Unlike the previously mentioned results at the pine forest or the Los Angeles area, the maximum amount of SOA formation in the OFR at T3 did not correlate well with any single SOA precursor gas, indicating the variable impacts of multiple sources.

If the assumption holds that VOCs and S/IVOCs from a given emission type correlate with each other, then a multivariate relationship should exist, where the measured SOA formation should correlate well with the sum of measured concentration of VOCs/tracers of each source, multiplied by coefficients. The coefficients would quantify the relative contributions to potential SOA from VOCs + S/IVOCs from each source, relative to the tracer. For this analysis, we used tracer gases that were likely to be dominated by a single type of source, including MT, SQT, and isoprene for biogenic emissions, NO_y for anthropogenic emissions, and the sum of the measured BB tracers (vanillin, vanillic acid, syringol, and guaiacol) for biomass burning emissions. A multilinear regression (MLR) analysis was performed to estimate the mass contributions to SOA formed in the OH-OFR for each of the source signatures.

The average amounts and fractions of total SOA formation estimated from each of the biogenic, anthropogenic, and BB sources during each season are shown in Figure 1.9. Averages of 1.50 and 2.53 μg m^{-3} were formed from ambient air during the wet and dry seasons for the times where data was available for SOA formation and all tracers. Of these amounts, 0.73 (48%), 0.67 (45%), and 0.10 (7%) μg m^{-3} during the wet season and 1.76 (69%), 0.30 (12%), and 0.47 (18%) μg m^{-3} during the dry season were attributed to biogenic, anthropogenic, and BB sources, respectively. These results indicate that biogenic SOA forming-gases were the most important contributors during both seasons. Anthropogenic sources contributed more than double the mass and nearly quadruple the fraction during the wet season compared to the dry season. BB sources of SOA-forming gases contributed almost five times more SOA mass during the dry season compared to the wet season.

These results suggests key differences between the average wet and dry season atmospheres. One hypothesis is that these differences could be related to changing ambient photochemistry between seasons. The 12-h average daytime solar irradiation during the wet season was 307 W m^{-2}, which was 23% less than the 398 W m^{-2} during the dry season and suggests that photochemistry in ambient air was slower during the wet season. The toluene:benzene ratio in ambient air at the T3 site was higher in the wet season (1.45) than the dry season (1.0). Since toluene reacts faster with OH radicals than benzene, a higher ratio in the wet season indicates "fresher" or less processed emissions arriving at T3 from the city of Manaus. With slower ambient photochemistry, more SOA precursor gases could have survived the transport from Manaus leading to higher amounts of SOA formation in the OFR. In the dry season, these gases may have already been oxidized in the atmosphere to form SOA en route to the T3 site, entering the OFR as OA and not contributing to potential SOA formation. The stronger photochemistry during the dry season should increase the biogenic S/IVOC to primary VOC ratio. Since the primary VOCs were very similar in both seasons, the higher biogenic S/IVOCs in the dry season could explain the larger potential SOA from that source. The very different spatial footprints of anthropogenic and biogenic emissions would then result in these different effects on potential SOA from each source at the T3 sites. These hypotheses should be tested with future modeling studies.

This analysis estimates the contributions from each of these three emission types to the SOA forming gases (measured and unmeasured) at the T3 site. This provides information about what types of SOA could form upon further oxidation of this air at or downwind of the T3 site. Importantly, this analysis does not provide information about what amounts or fractions of the pre-existing (i.e. ambient) OA measured at the T3 site came from each of these sources. To investigate the sources of OA that impact the site and others in Amazonia, PMF analysis or other tracer analysis can be done, and will surely be the subject of future manuscripts. However, it would seem likely that the biogenic and biomass burning potential SOA sources observed here would also be important in formation the OA on a regional scale, whereas the anthropogenic source type may be more intense in the Manaus plume (within approximately the first day of transport) and less important on a regional scale.

Objective 2

Test the hypothesis that new particles under natural conditions are produced as a result of evaporation of primary particles emitted by fungal spores as well as to investigate any shifts in this mechanism under pollution conditions, e.g., in consequence to the high concentrations of SO_2 in the pollution plume

Activities led by **Saewung Kim** (UC-Irvine, funded by DOE)

The Thermal Desorption Chemical Ionization Mass Spectrometer (TDCIMS) was deployed at T3 during both IOPs to measure the molecular composition of 10 to 100 nm diameter particles. The TDCIMS deployment was motivated by two main scientific objectives of GoAmazon2014/5. (1) The first objective of TDCIMS observations was to determine the source of new ambient nanoparticles in the Amazon. The hypothesis priori to measurements has been that potassium salts formed from the evaporation of primary particles emitted by fungal spores provides a unique and important pathway for new particle production in the Amazon basin. To explore this hypothesis, the TDCIMS records the positive ion mass spectra of sampled ambient particles. Laboratory tests performed using potassium salts show that the TDCIMS can detect potassium with high sensitivity. (2) For studying the interactions between anthropogenic and biogenic emissions, the TDCIMS quantified the composition of nanoparticles that nucleate from anthropogenic emissions in neighboring urban areas such as Manaus and the role of biogenic precursors in the growth of these particles. Coincident measurements of gas phase sulfuric acid (see next section of report) allowed the determination of the contribution of sulfuric acid condensation to nucleation and growth, which we could be compare to TDCIMS-derived nanoparticle composition to determine the fraction of growth that can be attributed to the uptake of organic compounds. The molecular composition of sampled particles can be used to attribute specific chemical species and mechanisms to growth, such as the condensation of low-volatility species or the oligomerization of α-dicarbonyl compounds.

As general statements, the data sets show that peaks in most detected compounds in ultrafine aerosol particles occur in "plumes" in early morning under stagnant-wind conditions. Ultrafine aerosol particles are primarily composed of oxidized and nitrogen-containing organics, the latter includes cyanate (from isocyanic acid), which is likely linked to biomass burning. Particulate "potassium episodes" are observed occasionally. The source of these is still not known.

More specifically, Figure 2.1 shows the daily profile of ultrafine particle concentration ($N_{10\text{-}100nm}$) and major ions observed by the TDCIMS during IOP1. Ultrafine particle number concentration (Figure 7a) has a small daily trend of peaking in the evening hours, with a minimum in the morning (8:00-10:00 local time). In contrast to this behavior, the peak concentration of many chemical species such as nitrogen-containing organic molecules (represented by the fragment ion cyanate, OCN^-, plot b) and oxygenated organic molecules (represented by hydrogen oxalate, $HC_2O_2^-$, plot c, and acetate, $C_2H_3O_2^-$, plot d) occurs in the early morning hours between 2:00 and 6:00 local time. Sulfate (represented by bisulfate, HSO_4^-) and potassium (K^+), which are key hypothesized species of new particle formation, are relatively

minor constituents during the time period of these observations, and they do not appear to exhibit any daily patterns (results not shown).

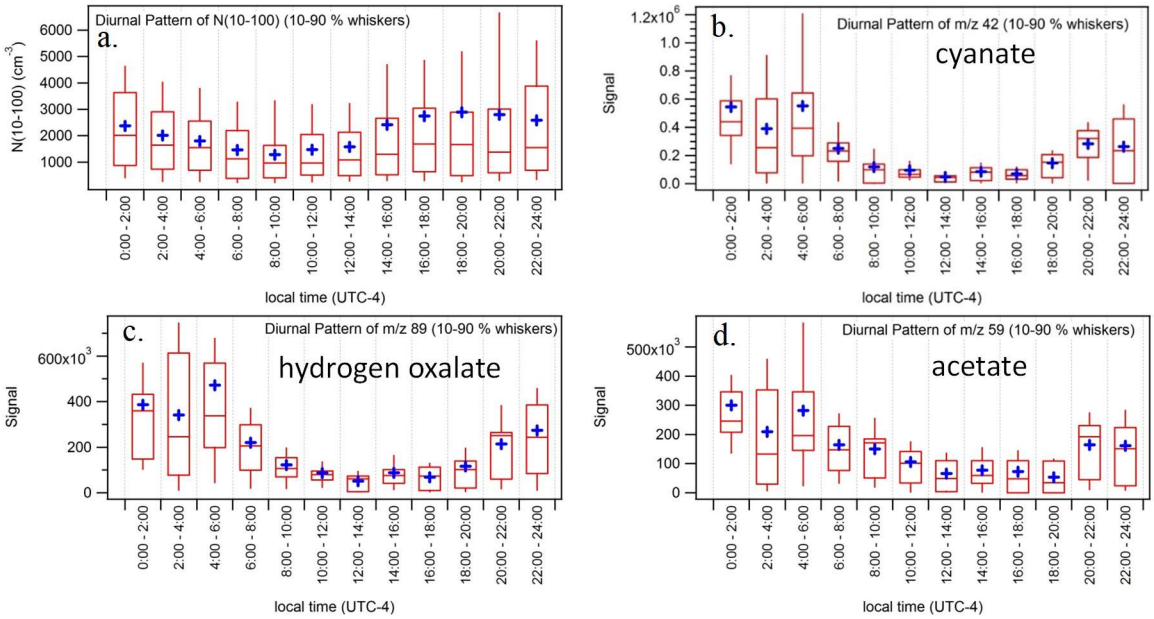

Figure 2.1. Daily profiles of ultrafine particle number concentration (a) and representative ions (b-d) during IOP1 of GoAmazon2014/15.

An interesting aspect shown in Figure 2.1 is that the clear diel pattern of acetate, cyanate, and oxalate, does not appear similar to the ultrafine particle concentration. One interpretation is that the constituents that cause the peak in the number concentration in the evening, between 16:00 and 24:00 (local time), are not detected by the TDCIMS. This possibility could include certain products of combustion such as long chain alkanes or PAHs that are not detectable by the chemical ionization reagents. A peak of the detected compounds in the early morning hours could be due to calm wind conditions during that time period and could be aided by a lower boundary layer that traps locally-produced ultrafine particles close to the ground.

In summary, low levels of sulfate observed in nanoparticles confirms that sulfur-containing compounds, such as sulfuric acid, are not important contributors to ultrafine particle growth in this region. High levels of *m*/*z* 42, which can be attributed to cyanate, suggest that compounds arising from biomass burning could play a major role in the formation of ultrafine particles in this region. This compound, which can be linked to health impacts such as cataracts and inflammation that can trigger cardiovascular disease and rheumatoid arthritis, has been observed previously in the gas phase. Low levels of potassium measured by the TDCIMS suggest that the fungal-spore mechanism for ultrafine particle formation could be restricted to certain environments rather than completely throughout the Amazon basin.

A chemical ionization mass spectrometer (CIMS) was deployed to T3 to quantify atmospheric H_2SO_4 and OH concentrations both IOPs. Both of these species are uncertain in Amazonia and represent key players in possible mechanisms of new particle production. A speculated explanation to the puzzling absence of new particle production in the Amazon basin, compared

to other continental regions, has been that H_2SO_4 concentration in the region would be below the necessary trigger threshold. This deployment makes the first measurements in the central Amazon basin.

Measurements of OH and H_2SO_4 for IOP1 are shown in Figure 2.2a. The daytime maxima for OH and H_2SO_4 concentrations were 1.5×10^6 molecules cm^{-3} and 1×10^6 molecules cm^{-3}, respectively. The OH concentrations were lower than previously reported for tropical rain forests (i.e., 2 to 6×10^6 molecules cm^{-3}). H_2SO_4 levels were significantly below the suggested threshold for the new particle production (i.e., 6×10^6 molecules cm^{-3}). These concentrations are, however, higher levels than model-calculated H_2SO_4 levels (e.g. 5×10^5 molecules cm^{-3}).

Measurements of OH and H_2SO_4 observations for IOP2 are shown in Figure 8b. Against initial expectations, both the OH and H_2SO_4 concentrations were lower in the dry season (IOP2) compared to the wet season (IOP1). Although it requires further investigations for the specific

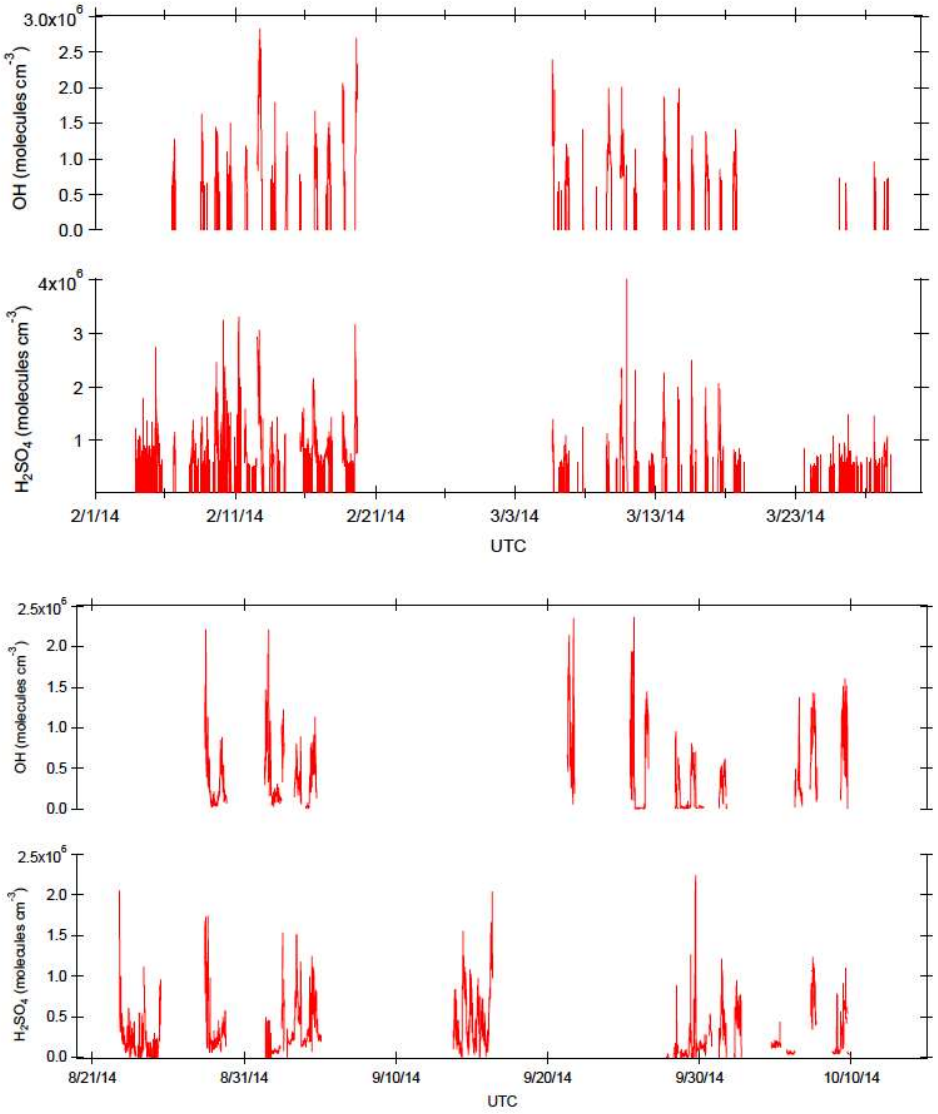

Figure 2.2. Time series of OH and H_2SO_4 concentrations during (top) IOP1 and (btm) IOP2.

causes behind of these observations, WRF-Chem (a regional chemistry modeling system) simulated this same trend between the wet and the dry seasons. It seems higher isoprene concentrations in the dry season is the main driver for the observations, at least for OH. The increased PM_1 surface area in IOP2 might provide an important sink for H_2SO_4 and explain its lower concentrations.

In additional analysis, we conducted investigations concerning the relative contribution of OH and sCI reaction channels to H_2SO_4 production. A global model calculation suggests that model-calculated H_2SO_4 is enhanced by a factor of about two once the sCI reaction channel is included. By comparison, our model results using an observationally constrained box model indicate it may contribute only 6 – 15 % of a local H_2SO_4 production. In summary, H_2SO_4 in the Amazon region was observed at measurable level although SO_2 as an important precursor was observed very low. For several sites worldwide, there is an approximately linear relationship between SO_2 and H_2SO_4 concentrations.

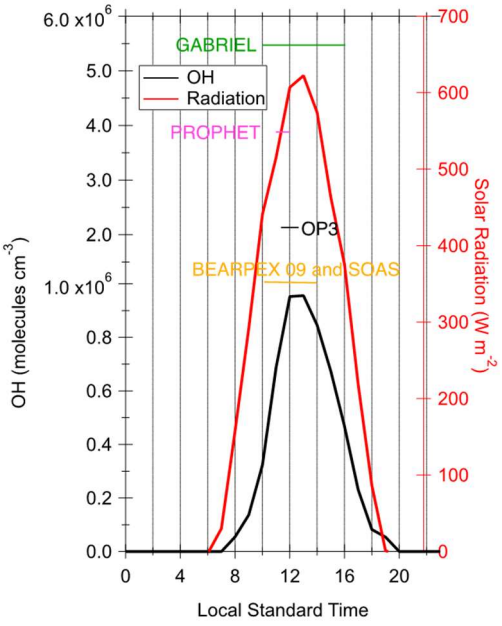

Figure 2.3. The daily averages of OH during the GoAmazon IOP I. It is an average over 22 days when OH observation was conducted.

An important motivation for the deployment of the CIMS for OH quantification was to resolve a controversy of higher than expected OH concentrations reported earlier for the Amazon region. Most of observation results from low NO_x-high isoprene environments such as clean rain forest cannot be accounted by conventional knowledge on OH-isoprene-NO_x oxidation photochemistry. Even so, most of those reports were from studies applying the laser induced fluorescence (LIF), and a need to verify the observations using an independent technique was raised in the community. For our data sets, the OH datasets both from wet and dry seasons do not show unexpectedly high concentrations and therefore do not support the thesis of the unaccounted recycling process maintaining oxidation capacity in low NO_X-high isoprene environments. The averaged daily variation of OH is shown in Figure 2.3 along with average OH concentrations from previous field observations with similar photochemical conditions – low NO and high isoprene concentrations. The observed OH concentrations during this campaign is significantly lower than those from previous campaigns utilized LIF instrumentation with wave modulation background characterization technique such as GABRIEL, PROPHET, and OP3. On the other hand, previous LIF observations with a chemical removal background characterization method such as BEARPEX-09 and SOAS show systematically lower OH, which is also consistent with CIMS observed OH from IOP 1.

We configured an observationally constrained box model to examine the observed OH specifically whether any additional recycling chemical mechanisms that previous studies have claimed would be necessary to account the observed OH. The chemical mechanisms were based on Master Chemical Mechanisms developed by University of Leeds. To evaluate different proposed isoprene oxidation mechanisms in low NO environments, we employed four different chemical mechanisms for the box model simulations. Two scenarios are based on isoprene photochemical mechanisms from MCM 3.1 (Scenario I) and MCM 3.2.1 (Scenario II). These scenarios are representing NO driven OH recycling a conventionally considered OH recycling mechanism predicting low OH concentrations in high isoprene and low NO environments. In addition, we employed two chemical mechanisms containing an excessive additional OH recycling mechanisms (Scenarios III and IV). The model simulation results along with the observed OH diurnal variation is shown in Figure 2.4. The model simulation results clearly are grouped in two- one with higher and the other with lower predicted OH. The observed OH diurnal variation can be certainly accounted by the OH variation simulated by Scenario I and Scenario II with a conventional OH recycling process. The results again illustrate that OH can be accounted using a conventional isoprene photochemical mechanism at the research site and during the given time frame that is an essential basis for evaluating secondary photochemical product formation rates.

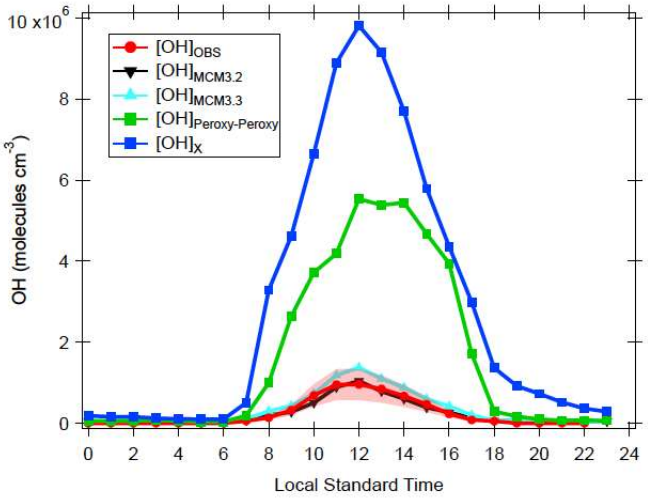

Figure 2.4. Box model simulated daily OH variations using the different model scenarios.

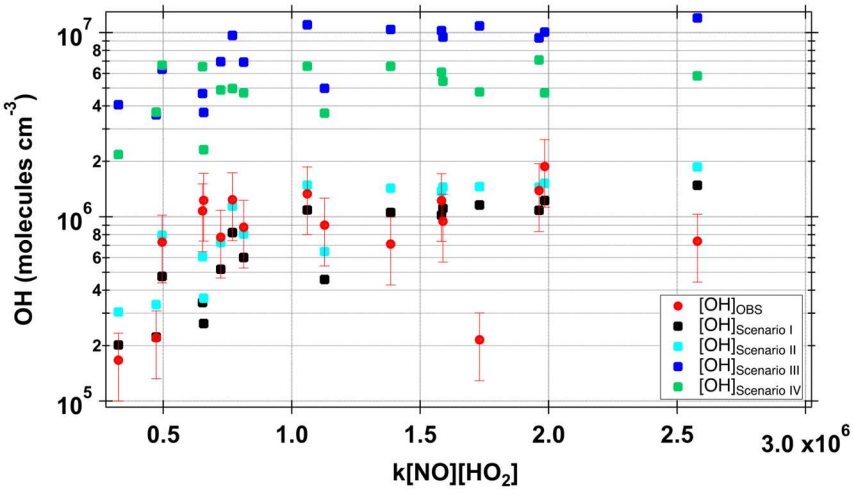

Figure 2.5. A correlation between observed and simulated OH and OH recycling rate from a reaction of HO_2 with NO.

Not only the analysis on the averaged diurnal variation on OH based on the 17-day observation but also the day by day OH variation is consistent with a conventional OH recycling mechanism. The T3 site, where the OH observation was conducted, had often been influenced by pollution plumes form Manaus, which certainly contained additional NO_X. In Figure 2.5, we presented averaged OH between 11:00 to 15:00

pm as a function of OH recycling rates from a reaction between NO and HO_2 considered the conventional recycling processes. As the site had been under the different levels of the pollution influences, the reaction rates between NO and HO_2 are evaluated in an extended range. It is very clear that isoprene photo-oxidation mechanisms without augmented OH recycling processes (e.g. Scenario I and II) well account observed OH in over the all reaction rates. It is worth noting that even isoprene photo oxidation mechanisms with augmented OH recycling (e.g. Scenario III and IV) illustrate OH decrease as the reaction rate between NO and HO_2 decreases. This observation does not support a claim on sustained oxidation capacity in high isoprene and low NO environments.

In summary, the first direct H_2SO4 (g) observation illustrated that the concentration was in general lower than the threshold to initiate new particle formation events but higher than global model estimates. CIMS observed OH was much lower than the previously observed OH in similar environments with LIF instrumentation equipped with a wave modulation background characterization system. A comprehensive box model evaluation illustrated that a conventional understanding on OH recycling without augmented OH recycling well accounts observed OH. This finding is consistent with recent LIF observation with improved background characterization system.

Objective 3

Upscaling to the effects of aerosol particles on clouds and climate under clean and pollution conditions

---

Part 1. Activities led by **Rodrigo Souza** (UEA, funded by FAPEAM)

The study evaluated how a changing energy matrix in a tropical, forested environment affects urban pollutant concentrations. In 2009, a 650 km natural gas pipeline was inaugurated, linking a region of natural gas production in Urucu, Amazonas, to Manaus, initiating a shift from fuel oil and diesel electrical park to natural gas. That change coupled to the GoAmazon2014/5 data sets represented a unique opportunity to evaluate how fuel switching can affect air quality, especially in regard to little-studied tropical forest environments. For that purpose, ozone was chosen for detailed study because of the concern for human health and the susceptibility of its secondary production to factors at play in a forest environment. The study provides interpretative context for the 2-year experiment of GoAmazon2014/5. For case A of the study, fuel oil and diesel were used for electricity production, which was the reality in 2008. The Urucu pipeline began initial, albeit small, shipments of natural gas in 2010, with increasing amounts every year thereafter. By 2014, natural gas had increased from 0 to 65% of the energy matrix for electricity production. Case B corresponded to the energy matrix of 2014. Case C considered the nearly complete use of natural gas for electricity production, which is the planned future, possibly for 2018. For each case, inventories of anthropogenic emissions were developed based on electricity generation, refining operations, and transportation. Transportation and refinery operations are held constant across the three scenarios to focus on effects of power plant fuel switching in a tropical context. The study

focused on the wet season because regional anthropogenic activities of the urban environment are easily compared to background conditions

Simulations were carried out using the Weather Research and Forecasting model fully coupled to a chemical module (WRF-Chem version 3.6.1). Two nested domains were employed. An outer domain had a resolution of 10 km and a dimension of 1050 km x 800 km. This domain employed reanalysis data from the Climate Forecast System Reanalysis (CFSv2). An inner domain had a resolution of 2 km and a dimension of 302 km x 232 km.

Figure 3.1 shows a box-and-whisker plot of ozone concentrations for all afternoons for each case. The time period of 12:00 to 16:00 (local time) was selected for analysis because it represents the maximum ozone concentration, which is fundamentally linked to photochemistry. For the statistical analysis of Figure 3.1, an area of 10 km x10 km centered on Manaus was taken to assess ozone concentrations in the populated urban area. The analysis represented in Figure 10 shows that within a single case ozone concentrations had large differences throughout the simulated month. These day-to-day differences arose largely because of variability in cloudiness and other meteorological components of the simulation. Some days were sunny, favoring the photochemical process of ozone formation, whereas other days were overcast or rainy. The variability in ozone concentrations apparent in Figure 3.1 among cases A, B, and C arose from differences in the energy matrix for electricity production. A partial shift from diesel and oil to natural gas (i.e., cases A and B) did not greatly shift ozone concentrations, on either polluted or clean days. A complete shift to natural gas (i.e., case C), however, considerably reduced ozone concentrations in the urban region. Maximum afternoon ozone concentrations on fair-weather days decreased by more than 70% (e.g., 110 to 30 ppb) for the three most polluted days of the simulated month, which occurred on fair-weather days. On poor-weather days, the additional pollution from Manaus contributed to small or negligible additional ozone production.

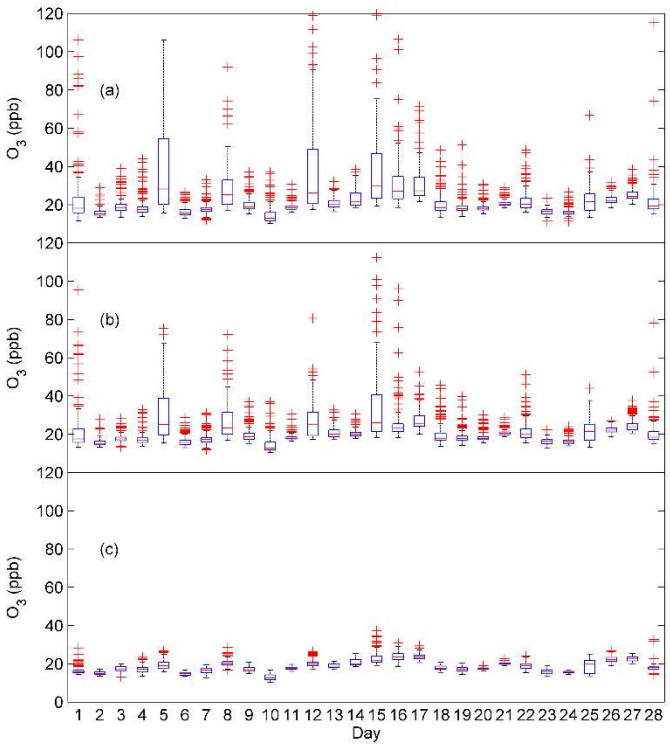

Figure 3.1. Box-and-whisker plot of near-surface ozone concentrations for historical emissions (case A), present-day emissions (case B), and planned future emissions (case C). On each day of the simulated month, the time period for the statistical analysis corresponds to 12:00 and 16:00 local time. The region of areal averaging is 10 km x 10 km, centered on 3.1° S, 60.0°W (boxed regions of Figures 1 and 3). The bottom and top of the blue boxes correspond to the first and third quartiles, respectively. The red line inside the box is the median. The whiskers represent the full range of values excluding outliers. The red crosses show outliers, as defined by more than 1.5 times the interquartile range.

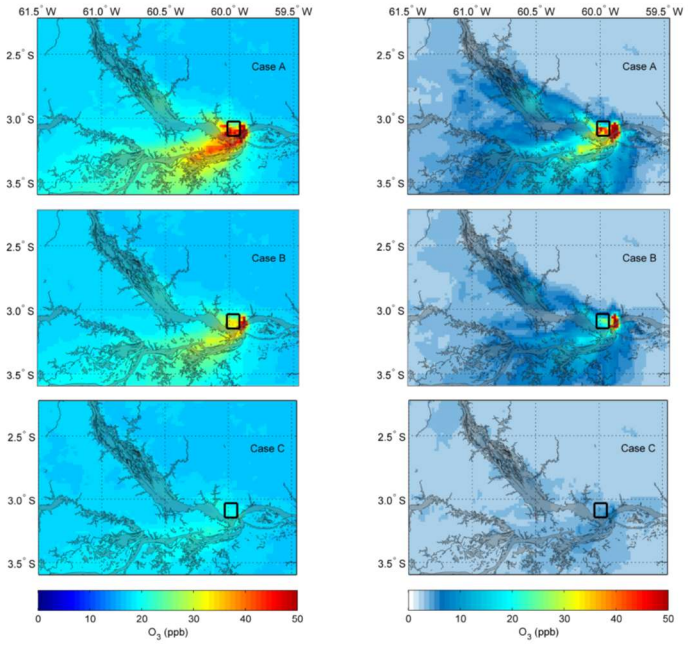

Figure 3.2. Maps of near-surface ozone concentrations for historic emissions (Case A), present-day emissions (Case B), and planned future emissions (Case C). The left column shows afternoon means for February 2014. The right column shows afternoon standard deviations. See caption of Figure 3 for further information.

The spatial distributions of the mean of afternoon values and their standard deviation over the full month of simulation are shown in Figure 3.2. The ozone plume spreads downwind from Manaus carried by the easterlies of the equatorial trade winds. The map shows that the pollution associated with Manaus emissions not only affects local air quality of the urban population but also reaches other regional downwind population centers, such as Careiro, Iranduba, and Manacapuru. The qualitative spatial pattern of the ozone plume is similar among cases A, B, and C, as explained by the use of identical meteorology. The concentrations, however, have strong differences. From cases A to B, the concentrations inside the plume do not differ greatly, in agreement with the box-and-whisker representation in Figure 3.2.

A comparison between measurements of NO_x and O_3 on board the G-1 aircraft over and downwind of Manaus during GoAmazon2014/5 and simulation results is presented in Figure 12 for case B. Figure 3.3a shows agreement between median and interquartile ranges of observed and simulated NOx concentrations. These concentrations above the natural regional background arise as primary pollutant in Manaus emissions. Likewise, simulated O_3 concentrations also show good agreement with aircraft data (Figure 3.3b). Ozone is a secondary pollutant, and the agreement supports the validity of the emission inventory of ozone precursors and the chemical mechanisms used in the simulation. Overall, the comparison shows that the simulations satisfactorily represent average regional afternoon concentrations of NO_x and O_3.

In summary, the results show that an altered energy matrix significantly influences air quality, as gauged by the maximum afternoon ozone concentration. The relationship between the Manaus emissions and the vast biogenic emissions of the surrounding forest constitutes an important scenario for studying feedback connections in atmospheric chemistry. The large differences between cases A and C show that the burning of fuel oil and diesel has a dominant role in regional ozone production. Conversely, substitution by natural gas greatly improves the outlook for regional air quality and human health. The results emphasize the high sensitivity of the atmospheric chemistry over the tropical forest to pollution, as amplified by the high solar irradiance and water vapor concentrations in an environment of plentiful biogenic VOC emissions.

Specifically, the significant decrease in NOx emissions from cases A to B resulted in no strong differences in ozone concentrations, whereas, conversely, the smaller increase from case C to B resulted in large ozone production. This nonlinear behavior of ozone concentration with respect to pollution is linked to the chemical cycles of the ozone production, more specifically to the domain of NO_x limitation or not.

The results suggest that the anticipated complete conversion to natural gas for electricity production should significantly reduce ozone concentration in the Manaus urban region. The GoAmazon2014/5 experiment occurred during two years of this ten-year transition in the energy matrix. Smaller municipalities throughout the Amazon Basin, which is two-thirds the size of the contiguous USA, continue to burn sulfur-laden oil and diesel for electricity production. Further changes in the energy matrix of Amazonia are dependent on continued development of infrastructure for use of natural gas or making connections to the national grid and continued developments in the use of hydropower, even as the population of Amazonia continues to grow rapidly.

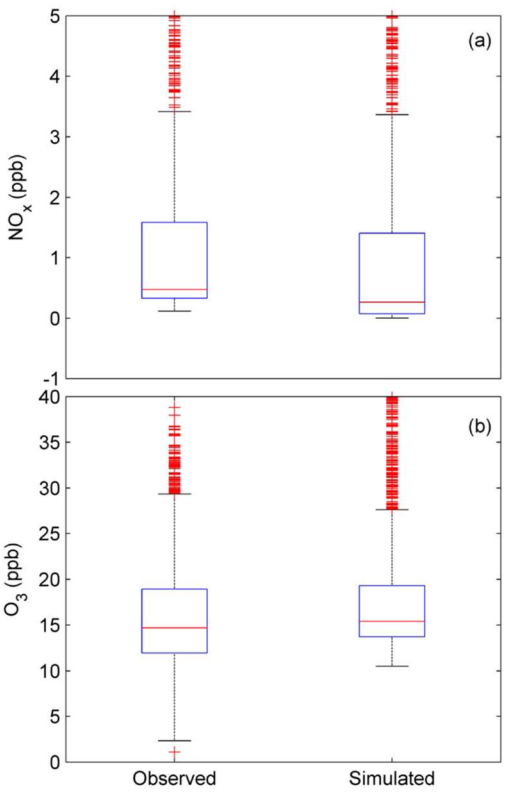

Figure 3.3. Box-whisker plots comparing observed and simulated (a) NOx concentrations and (b) ozone concentrations. Observation data were obtained from G-1 flights during six days of March 2014 during GoAmazon2014/5. There were no flight data from February 2014 applicable for comparison. The G-1 data correspond to an altitude window of 500 to 650 m high and an afternoon time window (11:00 to 15:00, local time; 15:00 to 19:00 UTC). Simulation data were selected from a similar vertical level and compatible flights paths and times. The simulation used the methodology described in Section 2 and emissions for Case B (real case). The comparison in the figure shows that there is good agreement in the range of simulated and observed ozone concentrations.

Part 2. Activities led by **Henrique Barbosa** (USP, FAPESP)

The activities focused on the scientific objective focuses on how variability in the number-diameter distribution of the particle population for natural and polluted conditions, as well as variability in the intrinsic effective hygroscopicity κ, of the particles affects cloud properties. To

investigate the condensational growth by water vapor deposition on aerosol particles, which is the main growth mechanism in the first stages of a warm cloud, we have implemented a adiabatic parcel model and used it to simulated clean and polluted conditions. This zero-dimensional adiabatic model, although very simple, does allow the simulation of the temporal evolution of the droplet spectra from a given aerosol size distribution and thermodynamic condition. It can accurately describe the activation of part of the aerosol population, as the parcel rises, correctly predicting the droplet concentration at cloud base. Such models also serve as a theoretical reference for parameterizations of droplet activation such as those included in atmospheric circulation models. The complexity of parcel models vary according to the range of physical processes one is willing to study. There are those more complex, which include chemical processes between the aqueous and gaseous phases, in addition to collision-coalescence, or even ice processes; and those simpler that only solve the equation for condensational growth, which is our case.

The model starts from an aerosol size-distribution and calculates its equilibrium with a specified ambient relative humidity, temperature and pressure. The air parcel rises with constant and prescribed vertical velocity without mixing with the environment. As it expands and cools, changes in relative humidity and temperature are calculated and aerosol particles are allowed to gain or lose water by condensation and evaporation. For an accurate description of the CCN activation, we use κ-Köhler model. Collision, coalescence and entrainment are not considered, as they can be neglected in the first stages of cloud formation. Validation of the model was accomplished by comparison with three cases found in the literature.

To investigate the influence of the Manaus pollution plume on the initial formation of shallow warm clouds, we performed a series of simulations with conditions varying from clean to pollute. Table 3.1 present initial conditions for clean compared to polluted conditions based on the measurements of GoAmazon2014/5. The parameters are plotted in Figure 3.4.

Table 3.1 – Summary of basic aerosol parameters used in the simulations. T0a data is average from Feb/2014 to May/2014, while T2 is average from Dec/2014 to Mar/2015.

Site	N_{CN} (cm^{-3})	Mode	N_{CN} (cm^{-3})	D_g (nm)	σ_g	$K_{a,m}$
T0a	391 ± 12	Nucleation				
		Aitken	246±9	70 ± 1	1.53 ± 0.01	0.13 ± 0.02
		Accumulation	145±8	170 ± 2	1.42 ± 0.01	0.21 ± 0.05
T2	2.544 ± 154	Nucleation	452±50	27.2 ± 0.1	1.27 ± 0.01	
		Aitken	1479 ± 121	51.8 ± 0.9	1.58 ± 0.04	0.07 ± 0.02
		Accumulation	613±81	139.4 ± 9.0	1.67 ± 0.05	0.09 ± 0.02

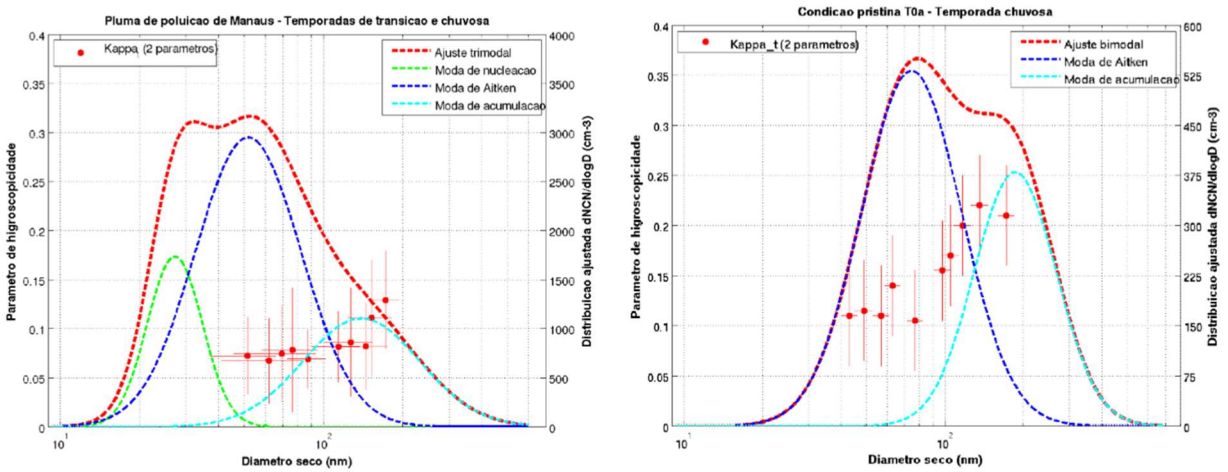

Figure 3.4. Aerosol size distribution measured at the polluted site T2 (left) and pristine site T0a (right) are shown as curves fitted for the nucleation mode (green), Aitken mode (blue) and accumulation mode (cyan). Data points are the size-resolved hygroscopicity and take values on the right axis.

Four simulation scenarios were considered. The scenarios were arranged with these single steps in increasing complexity because we know from previous studies which parameters have the most influence on the droplet radius and number concentration. For scenario 1 we used the pristine size distribution and average hygroscopicity. We scaled the size distribution to vary the total concentration from 100 to 10,000 cm^{-3}, and we varied the updraft velocity from 0.1 (typical of shallow clouds) to 10 m/s (typical of thunderstorms). For scenario 2, we further allowed the size distribution shape (D_g and σ_g) to change with the concentration. D_g and σ_g (for each mode) were linearly interpolated from the values measured at T0a when N_{CN} = 391 cm^{-3}, to the values measured at T2, when N_{CN} = 2544 cm^{-3}. For total concentrations lower (higher) than these limits, the shape parameters were those from T0a (T2). For scenario 3, we further allowed the average hygroscopicity parameter to vary from its mean value at T0z (0.14) when N_{CN} = 391 down to its mean value at T2 (0.08) when N_{CN} = 2544 cm^{-3}, and keeping it constant outside this range. For scenario 4, we further allowed the hygroscopicity parameter to vary with particle diameter.

Figures 3.5 and 3.6 show the results for the number of droplets activated (N_{CD}) and the activated fraction (N_{CD}/N_{CN}), respectively. For scenario 1, as expected, N_{CD} increases with N_{CN} and W. On the other hand, the activated fraction decreases with N_{CN} and increase with W. This is understood as following: for the same W, increasing N_{CN} means more particles will uptake water and hence the S_{max} will be lower. Lower S_{max} means a larger critical diameter, i.e., only larger particles will activate and hence the activated fraction will decrease as well. R_{eff} responds as N_{CD} because we are showing it at fixed liquid water content.

We consider the variation of the shape of the size distribution in addition to the total aerosol concentration in scenario 2. For polluted conditions (N_{CN} >1000 cm^{-3}) there is a significant reduction in N_{CD} of about 1/3, and consequently S_{max} reaches higher values. The activated fraction, however, still decreases because the number of particles in the nucleation mode increases faster than the decrease in the critical diameter. R_{eff} increases by about 15% because the number of droplets activated decreased and we are comparing R_{eff} at fixed liquid water content. These large differences between scenario 1 and 2 show the variation of the size distribution shape should not be neglected.

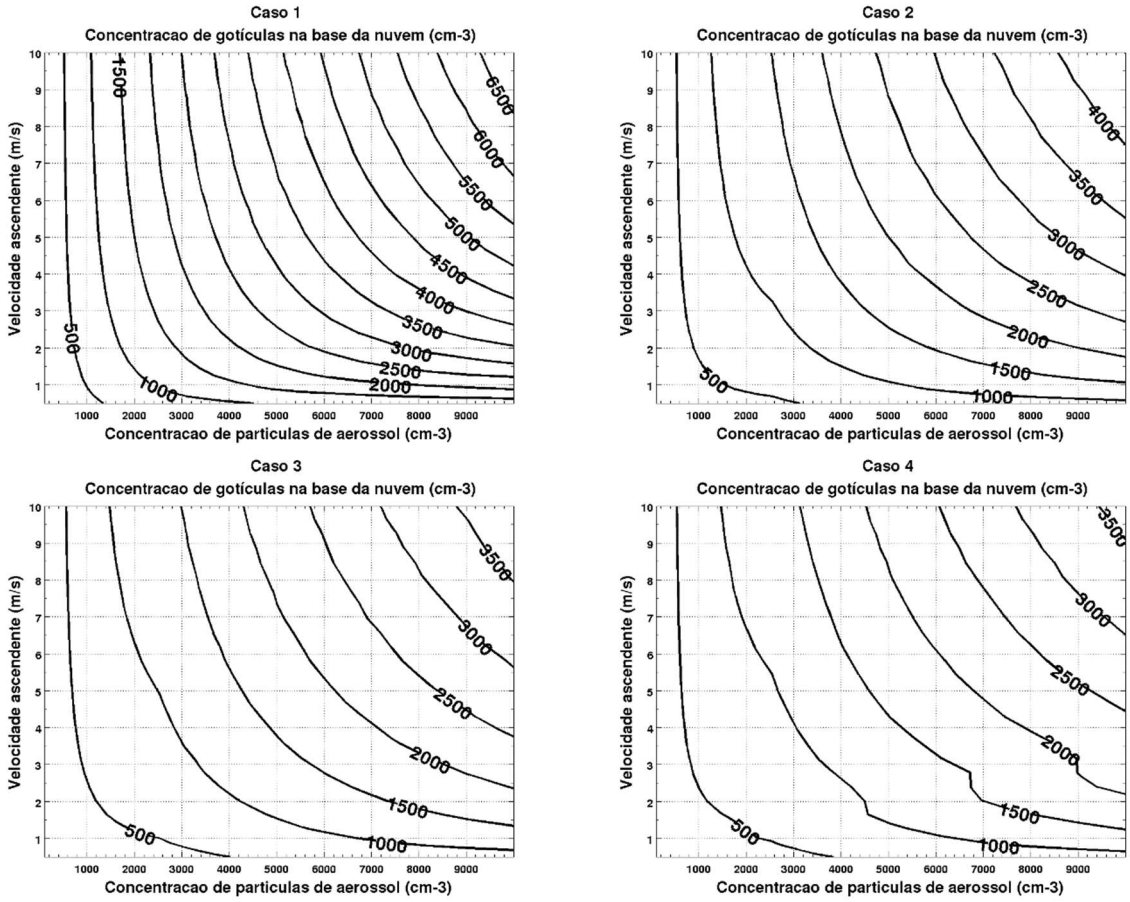

Figure 3.5. Droplet concentration at cloud base for scenarios 1 to 4 are shown.

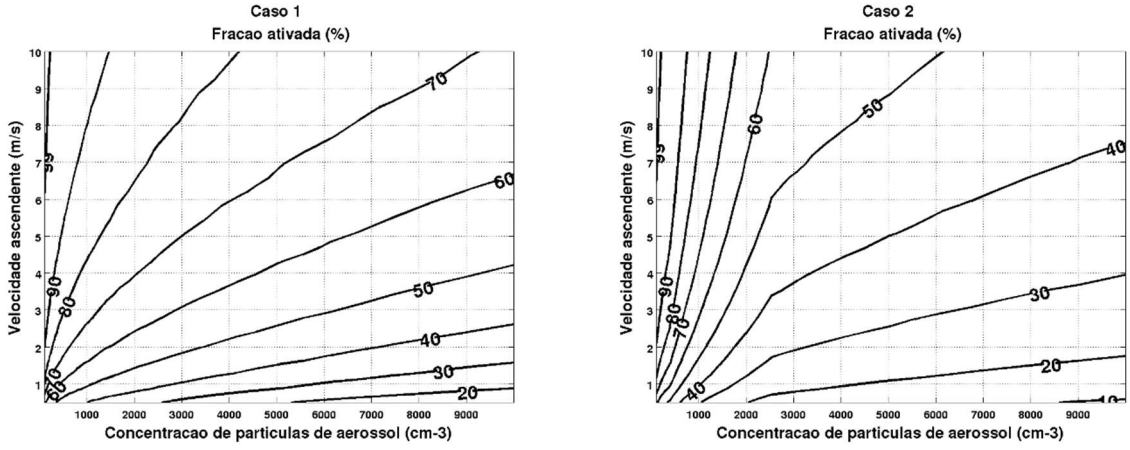

Figure 3.6. Activated fraction for scenarios 1 to 4 are shown.

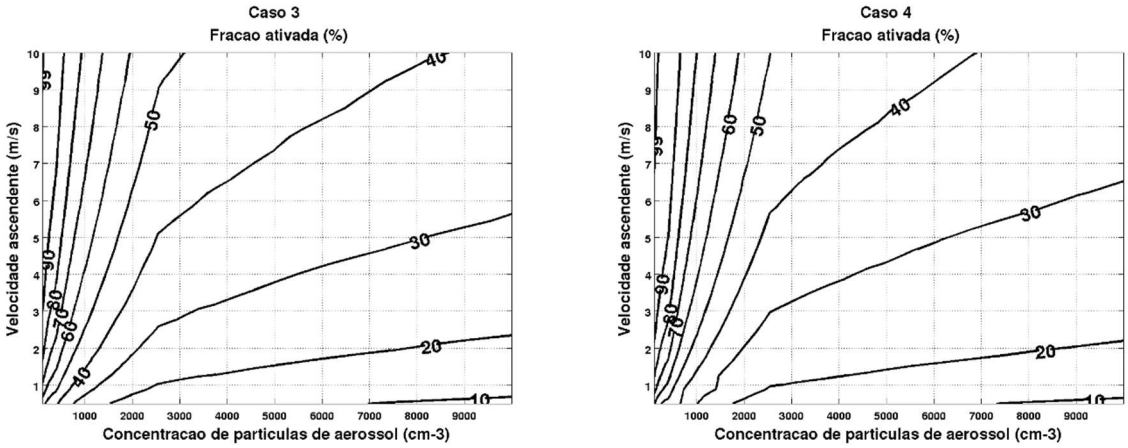

Figure 3.6 (cont'd). Activated fraction for scenarios 1 to 4 are shown.

We further considered the variation of the average hygroscopicity from 0.14 (pristine) to 0.08 (polluted) values in scenario 3. As expected, the number of activated droplets decreases even further, but only about 15%, as so does the activated fraction. S_{max} and R_{eff} increase but by only 8%. We see indeed that the change in hygroscopicity when going from pristine to polluted conditions is less important than the changes in the shape of the size distribution and, of course, in the total concentration. The last scenario was to consider the variation of hygroscopicity with size. The trend continues with lower N_{CD} and activated fraction and higher S_{max} and R_{eff}. The changes, however, are minor, of the order of a few percent.

List of publications (published, in peer review, or in preparation)

Published or Accepted

- S.T. **Martin**, P. Artaxo, L.A.T. Machado, A.O. Manzi, R.A.F. **Souza**, C. Schumacher, J. Wang, M.O. Andreae, H.M.J. **Barbosa**, J. Fan, G. Fisch, A.H. Goldstein, A. Guenther, J.L. **Jimenez**, U. Pöschl, M.A. Silva Dias, J.N. Smith, M. Wendisch. Introduction: Observations and Modeling of the Green Ocean Amazon (GoAmazon2014/5). *Atmos. Chem. and Phys.*, 16, 4785-4797, doi:10.5194/acp-16-4785-2016, 2016. https://www.atmos-chem-phys.net/16/4785/2016

- S.T. **Martin**, P. Artaxo, L. Machado, A.O. Manzi, R.A.F. **Souza**, C. Schumacher, J. Wang, T. Biscaro, J. Brito, A. Calheiros, K. Jardine, A. Medeiros, B. Portela, S. de Sá, K. Adachi, A.C. Aiken, R. Albrecht, L. Alexander, M.O. Andreae, H.M.J. **Barbosa**, P. Buseck, D. Chand, J.M. Comstock, D.A. Day, M. Dubey, J. Fan, J. Fast, G. Fisch, E. Fortner, S. Giangrande, M. Gilles, A.H. Goldstein, A. Guenther, J. Hubbe, M. Jensen, J.L. **Jimenez**, F.N. Keutsch, S. **Kim**, C. Kuang, A. Laskin, K. McKinney, F. Mei, M. Miller, R. Nascimento, T. Pauliquevis, M. Pekour, J. Peres, T. Petäjä, C. Pöhlker, U. Pöschl, L. Rizzo, B. Schmid, J.E. Shilling, M.A. Silva Dias, J.N. Smith, J.M. Tomlinson, J. Tóta, M. Wendisch. The Green Ocean Amazon Experiment (GoAmazon2014/5) Observes Pollution Affecting Gases, Aerosols, Clouds, and Rainfall over the Rain Forest. *Bulletin of the*

American Meteorological Society (BAMS), 98, 981–997, doi:10.1175/BAMS-D-15-00221.1, 2016. http://journals.ametsoc.org/doi/abs/10.1175/BAMS-D-15-00221.1

- Wang, J., Radovan Krejci, Scott Giangrande, Chongai Kuang, Henrique M. J. **Barbosa**, Joel Brito, Samara Carbone, Xuguang Chi, Jennifer Comstock, Florian Ditas, Jost Lavric, Hanna E. Manninen, Fan Mei, Daniel Moran-Zuloaga, Christopher Pöhlker, Mira L. Pöhlker, Jorge Saturno, Beat Schmid, Rodrigo A. F. **Souza**, Stephen R. Springston, Jason M. Tomlinson, Tami Toto, David Walter, Daniela Wimmer, James N. Smith, Markku Kulmala, Luiz A. T. Machado, Paulo Artaxo, Meinrat O. Andreae, Tuukka Petäjä, and Scot T. **Martin**, 2016: Vertical transport during rainfall sustains aerosol concentration in Amazon boundary layer. Nature, doi:10.1038/nature19819.

- Liu, Y., Brito, J., Dorris, M. R., Rivera-Rios, J. C., Seco, R., Bates, K. H., Artaxo, P., Duvoisin, S., Keutsch, F. N., **Kim**, S., Goldstein, A. H., Guenther, A. B., Manzi, A. O., **Souza**, R. A. F., Springston, S. R., Watson, T. B., McKinney, K. A., and **Martin**, S. T.: Isoprene photochemistry over the Amazon rain forest, Proc. Natl. Acad. Sci. USA, 113, 6125-6130, 2016, 10.1073/pnas.1524136113.

- Bateman, A.P., Gong, Z., Liu, P., Sato, B., Cirino, G., Zhang, Y., Artaxo, P., Bertram, A. K., Manzi, A. O., Rizzo, L. V., **Souza**, R. A. F., Zaveri, R. A., **Martin**, S.T., Submicron particulate matter is primarily in liquid form over Amazon rain forest, *Nature Geoscience*, 2016, *9*, 34-37.

- W.W. Hu, P. Campuzano-Jost, B.B. Palm, D.A. Day, A.M. Ortega, P.L. Hayes, J.E. Krechmer, Q. Chen, M. Kuwata, Y.J. Liu, S.S. de Sá, K. McKinney, S.T. **Martin**, M. Hu, S.H. Budisulistiorini, M. Riva, J.D. Surratt, J.M. St. Clair, G. Isaacman-Van Wertz, L.D. Yee, A.H. Goldstein, S. Carbone, J. Brito, P. Artaxo, J.A de Gouw, A. Koss, A. Wisthaler, T. Mikoviny, T. Karl, L. Kaser, W. Jud, A. Hansel, K.S. Docherty, M.L. Alexander, N.H. Robinson, H. Coe, J.D. Allan, M.R Canagaratna, F. Paulot, and J.L. **Jimenez**. Characterization of a Real-Time Tracer for Isoprene Epoxydiols-Derived Secondary Organic Aerosol (IEPOX-SOA) from Aerosol Mass Spectrometer Measurements. *Atmos. Chem. Phys.*, 15, 11807-11833, doi:10.5194/acp-15-11807-2015, 2015. http://www.atmos-chem-phys.net/16/11563/2016

- W.W. Hu, B.B. Palm, D.A. Day, P. Campuzano-Jost, J.E. Krechmer, Z. Peng, S.S. de Sá, S.T. **Martin**, M.L. Alexander, K. Baumann, L. Hacker, A. Kiendler-Scharr, A.R. Koss, J. de Gouw, A.H. Goldstein, R. Seco, S.J Sjostedt, J.-H. Park, A.B. Guenther, S. **Kim**, F. Canonaco, A.S.H. Prévôt, W.H. Brune, J.L. **Jimenez**. Volatility and lifetime against OH heterogeneous reaction of ambient Isoprene-Epoxydiols-Derived Secondary Organic Aerosol (IEPOX-SOA). *Atmos. Chem. and Phys.*, 16, 11563-11580, doi:10.5194/acp-16-11563-2016, 2016. http://www.atmos-chem-phys.net/16/11563/2016

- A.P. Bateman, Z. Gong, T.H. Harder, S.S. de Sá, B. Wang, P. Castillo, S. China, Y. Liu, R.E. O'brien, B.B. Palm, H.-W. Shiu, G.G. Cirino, R. Thalman, K. Adachi, M. L. Alexander, P. Artaxo, A.K. Bertram, P.R. Buseck, M.K. Gilles, J.L. **Jimenez**, A. Laskin, A.O. Manzi, A. Sedlacek, R.A.F. **Souza**, J. Wang, R. Zaveri, and S.T. **Martin**. Anthropogenic influences on

the physical state of submicron particulate matter over a tropical forest. *Atmos. Chem. Phys.*, 17, 1759-1773, doi:10.5194/acp-17-1759-2017, 2017. https://www.atmos-chem-phys.net/17/1759/2017

- G. Isaacman-VanWertz, L.D. Yee, N.M. Kreisberg, R. Wernis, J.A. Moss, S.V. Hering, S.S. de Sá, S.T. **Martin**, M.L. Alexander, B.B. Palm, W. Hu, P. Campuzano-Jost, D.A. Day, J.L. **Jimenez**, M. Riva, J.D. Surratt, J. Viegas, A.O. Manzi, E.S. Edgerton, K. Baumann, R.A.F. **Souza**, P. Artaxo, A.H. Goldstein. Observed ambient gas-particle partitioning of tracers for biogenic oxidation. *Environmental Science & Technology,* 50, 9952–9962, doi:10.1021/acs.est.6b01674, 2016. http://pubs.acs.org/doi/abs/10.1021/acs.est.6b01674

- S.S. de Sá, B.B. Palm, P. Campuzano-Jost, D.A. Day, M.K. Newburn, W. Hu, G. Isaacman-VanWertz, L.D. Yee, R. Thalman, J. Brito, S. Carbone, P. Artaxo, A.H. Goldstein, A.O. Manzi, R.A.F. **Souza**, F. Mei, J.E. Shilling, S.R. Springston, J. Wang, J.D. Surratt, M.L. Alexander, J.L. **Jimenez**, and S.T. **Martin**. Influence of urban pollution on the production of organic particulate matter from isoprene epoxydiols in central Amazonia. *Atmos. Chem. Phys.*, 17, 6611-6629, https://doi.org/10.5194/acp-17-6611-2017, 2017. https://www.atmos-chem-phys.net/17/6611/2017

- Peng, Z., Day, D. A., Stark, H., Li, R., Lee-Taylor, J., Palm, B. B., Brune, W. H., and **Jimenez**, J. L.: HOx radical chemistry in oxidation flow reactors with low-pressure mercury lamps systematically examined by modeling, Atmos. Meas. Tech., 8, 4863-4890, https://doi.org/10.5194/amt-8-4863-2015, 2015.

- Peng, Z., Day, D. A., Ortega, A. M., Palm, B. B., Hu, W., Stark, H., Li, R., Tsigaridis, K., Brune, W. H., and **Jimenez**, J. L.: Non-OH chemistry in oxidation flow reactors for the study of atmospheric chemistry systematically examined by modeling, Atmos. Chem. Phys., 16, 4283-4305, https://doi.org/10.5194/acp-16-4283-2016, 2016.

- M. Shrivastava, J. Thornton, C. Cappa, J. Fan, A. Goldstein, A. Guenther, J.L. **Jimenez**, C. Kuang, A. Laskin, S. **Martin**, N.L. Ng, T. Petaja, J. Pierce, P. Rasch, P. Roldin, J. Seinfeld, J. Shilling, J. Smith, R. Volkamer, J. Wang, D. Worsnop, R. Zaveri, A. Zelenyuk, Q. Zhang. Recent advances in understanding secondary organic aerosols: implications for global climate forcing. Rev. Geophys., 55, 509–559, doi:10.1002/2016RG000540, 2017.

- Medeiros, Adan S. S., Calderaro, G., Guimarães, P. C., Magalhães, M. R., Morais, M. V. B., Rafee, S. A. A., Ribeiro, I. O., Andreoli, R. V., Martins, J. A., Martins, L. D., **Martin**, Scot T., **Souza**, R. A. F. Power Plant Fuel Switching and Air Quality in a Tropical Forested Environment. *Atmospheric Chemistry and Physics*, 17, 8987-8998, 2017.

- Sameh, A. A. R., Leila D. Martins, Ana B. Kawashima, Daniela S. Almeida, Marcos V. B. Morais, Rita V. A. **Souza**, Maria B. L. Oliveira, Rodrigo A. F. **Souza**, Adan S. S. Medeiros, Viviana Urbina, Edmilson D. Freitas, Scot T. **Martin**, and Jorge A. Martins. Mobile and stationary sources of air pollutants in the Amazon rainforest: a numerical study with WRF-Chem model. Atmospheric Chemistry and Physics, 17, 7977–7995, 2017.

- Ivan Kourtchev, Ricardo H. M. Godoi, Sarah Connors, James G. Levine, Alex T. Archibald, Ana F. L. Godoi, Sarah L. Paralovo, Cybelli G. G. **Barbosa**, Rodrigo A. F. **Souza**, Antonio O. Manzi, Roger Seco, Steve Sjostedt, Jeong-Hoo Park, Alex Guenther, Saewung **Kim**, James Smith, Scot T. **Martin**, and Markus Kalberer. Molecular composition of organic aerosols in central Amazonia: an ultra-high-resolution mass spectrometry study. Atmos. Chem. Phys., 16, 11899-11913, 2016.

- Cecchini, M. A., Machado, L. A. T., Comstock, J. M., Mei, F., Wang, J., Fan, J., Tomlinson, J. M., Schmid, B., Albrecht, R., **Martin**, S. T., and Artaxo, P.: Impacts of the Manaus pollution plume on the microphysical properties of Amazonian warm-phase clouds in the wet season, Atmos. Chem. Phys., 16, 7029-7041, doi:10.5194/acp-16-7029-2016, 2016.

- R. Thalman, S.S. de Sá, B.B. Palm, H.M.J. **Barbosa**, M.L. Pöhlker, M.L. Alexander, J. Brito, S. Carbone, P. Castillo, D.A. Day, C. Kuang, A. Manzi, N.L. Ng, A.J. Sedlacek, R.A.F. **Souza**, S.R. Springston, T.B. Watson, C. Pöhlker, U. Pöschl, M.O. Andreae, P. Artaxo, J.L. **Jimenez**, S.T. **Martin**, J. Wang. CCN activity and organic hygroscopicity of aerosols downwind of an urban region in central Amazonia: Seasonal and diel variations and impact of anthropogenic emissions. *Atmos. Chem. Phys. Discuss*., doi:10.5194/acp-2017-251, in review, 2017. https://www.atmos-chem-phys-discuss.net/acp-2017-251/.

In preparation

- A report on the composition of PM1 and source apportionment of organic material, revealing changes to PM_1 caused by Manaus pollution in the wet season is planned for de Sá et al., (**Martin**, PI)

- A report on the composition of PM1 and source apportionment of organic material, revealing changes to PM_1 caused by Manaus pollution and basin-wide biomass burning in the dry season is planned for de Sá et al., (**Martin**, PI)

- B.B. Palm, S.S. de Sá, D.A. Day, P. Campuzano-Jost, W.W. Hu, R. Seco, S.J. Sjostedt, J. Park, A.B. Guenther, S. **Kim**, J.F. Brito, F. Wurm, P. Artaxo, R.D. Thalman, J. Wang, L.D. Yee, R. Wernis, G. Isaacman-VanWertz, A.H. Goldstein, Y. Liu, S.R. Springston, R.A.F. **Souza**, M.K. Newburn, M.L. Alexander, S.T. **Martin**, and J.L. **Jimenez**. Secondary organic aerosol formation from ambient air in an oxidation flow reactor during GoAmazon2014/5, *In prep*, to be submitted August, 2017.

- L.D. Yee, G. Isaacman-VanWertz, R.A. Wernis, M. Meng, V. Rivera, N.M. Kreisberg, S.V. Hering, M.S. Bering, M. Glasius, M.A. Upshur, R.J. Thomson, F.M. Geiger, J.H. Offenberg, M. Lewandowski, I. Kourtchev, M. Kalberer, S.S. de Sá, S.T. **Martin**, M.L. Alexander, B.B. Palm, W.W. Hu, P. Campuzano-Jost, D. A. Day, J. L. **Jimenez**, Y. Liu, K.A. McKinney, J.F. Brito, P. Artaxo, J. Viegas, A.O. Manzi, M.B. Oliveira, R.A.F. de **Souza**, L.A.T. Machado, K.M. Longo, and A.H. Goldstein. Observations of sesquiterpenes and their oxidation products during GoAmazon 2014/5, *In prep*, to be submitted August, 2017.

- D. Jeong, R. Seco, Y. Liu, K. A. Mckinney, S. **Martin**, F. N. Keutsch, D. Gu, A. Guenther,

and S. **Kim**, Reconciling observed and predicted tropical rainforest OH concentrations using a Chemical Ionization Mass Spectrometer during the GoAmazon field campaign, In prep, to be submitted in August, 2017.

- S. **Kim** et al. Observations of H_2SO_4(g) during the GoAmazon campaign In prep